Main Manuscript for

Deforestation as an anthropogenic driver of mercury pollution

Aryeh Feinberg[a], Martin Jiskra[b], Pasquale Borrelli[c], Jagannath Biswakarma[b,d], and Noelle E. Selin[a,e]

[a] *Institute for Data, Systems, and Society, Massachusetts Institute of Technology, Cambridge, MA, USA*

[b] *Environmental Geosciences, University of Basel, Basel, Switzerland*

[c] *Department of Science, Roma Tre University, Rome, Italy*

[d] *Department of Water Resources and Drinking Water, Eawag, Dübendorf, Switzerland*

[e] *Department of Earth, Atmospheric, and Planetary Sciences, Massachusetts Institute of Technology, Cambridge, MA, USA*

*Correspondence to: arifeinberg@gmail.com (A.F.); martin.jiskra@gmail.com (M.J.)

Author Contributions: All authors conceived the study. M.J., J.B., and A.F. compiled Hg field data through literature review. A.F. and P.B performed the simulations. All authors contributed to the data analysis. A.F. wrote the draft of the paper with contributions and revisions from all authors.

Competing Interest Statement: The authors declare no competing interests.

Classification: Physical Sciences/Earth, Atmospheric, and Planetary Sciences

Keywords: mercury cycling; deforestation; emissions; chemistry-transport model.

This PDF file includes:

Main Text
Figures 1 to 4

Abstract

Deforestation reduces the capacity of the terrestrial biosphere to take up the toxic heavy metal mercury (Hg) and enhances the release of secondary Hg from soils. The consequences of deforestation on Hg cycling are not currently considered by anthropogenic emissions inventories or specifically addressed under the global Minamata Convention on Mercury. We use global Hg modeling constrained by field observations to quantify the impact of forest cover changes on the Hg cycle. We estimate that net atmospheric Hg fluxes due to deforestation are 217 Mg yr^{-1} (95% confidence interval, CI: 134–1650 Mg yr^{-1}) for 2015, approximately 10% of global primary anthropogenic emissions. In specific countries within the tropics, deforestation is a major source of anthropogenic Hg and can even exceed primary emissions. Land use policy will be a major control on future Hg emissions due to deforestation. For example, if deforestation of the Amazon rainforest continues at business-as-usual rates, net Hg emissions from the region will increase by 153 Mg yr^{-1} by 2050 (CI: 97–418 Mg yr^{-1}), enhancing the transport and subsequent deposition of Hg to aquatic ecosystems. We calculate the potential for substantial Hg emissions reductions for two cases of land use policies: conservation of the Amazon rainforest (92 Mg yr^{-1}, CI: 59 to 234 Mg yr^{-1}) and global reforestation (98 Mg yr^{-1}, CI: 64 to 449 Mg yr^{-1}). We conclude that deforestation-related emissions should be incorporated as an anthropogenic source in Hg inventories, and that land use policy could be leveraged to address global Hg pollution.

Significance Statement

Through deforestation, humans disrupt the storage of mercury (Hg) on land. This leads to more Hg entering aquatic ecosystems, where it can bioaccumulate to toxic levels in fish. Using available observations and modeling, we estimate that emissions of Hg driven by deforestation are approximately 10% of primary anthropogenic emissions, highlighting a source of Hg that has been previously overlooked. For countries in tropical regions, Hg emissions from deforestation can be a larger source than primary emissions. In the future, primary anthropogenic Hg emissions are expected to decline due to global policy efforts. Mercury emissions from land use change will therefore become more significant if deforestation continues at its current pace and should be addressed by policymakers and scientific assessments.

Main Text

Introduction

Humans are exposed to the organic form of mercury (Hg), methylmercury (MeHg), mainly through seafood consumption (1). Methylmercury is a potent neurotoxin, impairing the neurodevelopment of fetuses and children and costing the global economy $20–117 billion annually according to some estimates (2, 3). Mercury is emitted to the atmosphere by: a) primary anthropogenic sources, including artisanal and small-scale gold mining (ASGM), fossil fuel combustion, and metal smelting; b) re-emissions of historical anthropogenic (“legacy”) Hg from ocean and land; and c) geogenic sources (4). Mercury spreads globally in the atmosphere due to its long lifetime of 4–6 months (5). A global treaty, the Minamata Convention on Mercury, aims to protect human health and the environment from anthropogenic emissions and releases of Hg. The Convention’s measures target primary anthropogenic emissions sources by phasing out Hg use and adopting best available technologies for pollution control (6). However, primary anthropogenic emissions account for only 30% of present-day total emissions, with legacy re-emissions from land and ocean accounting for 60% (7). The future of Hg pollution will depend not only on reducing direct emissions through the Minamata Convention, but also on indirect anthropogenic influences on legacy Hg emissions and fate.

Terrestrial ecosystems, and especially forests, are important sinks of Hg from the atmosphere, taking up an estimated 2200–3600 Mg Hg per year (8), more than a third of total (anthropogenic, legacy, and geogenic) Hg emissions (7400 Mg yr^{-1}) (9). By taking up Hg, terrestrial ecosystems reduce the burden of Hg depositing in oceans, where it can be converted to MeHg and

bioaccumulated in fish. Previous studies have drawn useful analogies between Hg and carbon cycling in terrestrial ecosystems (10, 11). Like carbon dioxide (CO_2), elemental mercury (Hg^0) is assimilated by foliage throughout the growing season (12). Mercury is transported from the canopy to soil by foliage falling to the ground ("litterfall") and being washed off by precipitation ("throughfall"), which together are the major source (60–90%) of Hg in soils (8). Anthropogenic land use and land cover changes (LULCC), including deforestation, perturb both CO_2 and Hg fluxes to the atmosphere (13–15). In the case of carbon, scientific assessments (14) have calculated the contribution of LULCC to total CO_2 emissions (13% of total), and land management practices are governed by Article 5 of the Paris Agreement (16). For Hg, on the other hand, quantitative information related to the overall importance of land cover change is limited. Only one previous study modeled the impact of future LULCC on atmospheric Hg cycling, focusing on the effects of climate-induced changes to vegetation (15). No anthropogenic Hg emissions inventories have quantified the impacts of historical and future deforestation, and land management is not currently addressed by Hg policy efforts like the Minamata Convention.

Several processes mobilize Hg from terrestrial systems after deforestation. Along with removing a strong atmospheric sink of Hg (8), deforestation leads to more insolation reaching the soil, increasing photo-reduction and volatilization of Hg from soils (17). Fire-mediated deforestation leads to direct emission of Hg from forest and soil biomass (18). Soils in deforested areas are subject to accelerated erosion rates, enhancing Hg export to downstream ecosystems (19–21). Direct measurement of deforestation-driven fluxes at larger scales is challenging given variations in the land sink due to trends in environmental conditions, necessitating the use of models to quantify these fluxes (22). Models of terrestrial–atmosphere Hg fluxes, while still being much more uncertain than similar carbon cycle models, are improving due to a better process understanding and increasing availability of terrestrial measurements (8, 12, 23, 24). Thus, the time is ripe for assessing the relative importance of deforestation-driven fluxes in the Hg cycle.

Policies on local, national, and international scales will shape the future evolution of deforestation Hg fluxes. Deforestation due to agricultural land conversion threatens the Amazon rainforest (25, 26), which currently contributes 29% of the global land sink for atmospheric Hg^0 (23). At current deforestation rates, 40% of the Amazon rainforest could be lost by 2050, while enhanced environmental legislation (e.g., expansion of protected areas and enforcement) can reduce the deforested area to 15% (27). Reforestation and afforestation on the global scale are being studied as part of the solution to reach net zero greenhouse gas emissions in the future (28), though the efficacy of these measures has been debated (29). In any case, the climate mitigation benefits of forestation would not be realized without accompanying aggressive CO_2 emissions reductions (29, 30). Similarly, forest conservation and reforestation policies may have potential benefits for Hg sequestration on land, yet the magnitude of impacts remain unquantified.

Here, we apply the GEOS-Chem Hg model (23) to calculate deforestation emission factors for Hg from different regions and evaluate them against available observations. We quantify the global atmospheric Hg fluxes in 2015 that result from deforestation (217 Mg yr^{-1}; 95% confidence interval, CI: 134–1650 Mg yr^{-1}). We study the impact of future Amazon deforestation policy scenarios (27) and potential global reforestation efforts (30) on the terrestrial Hg sink. The magnitude of potential emissions reductions from Amazon conservation (92 Mg yr^{-1}; CI: 59–234 Mg yr^{-1}) and global reforestation (98 Mg yr^{-1}; CI: 64–449 Mg yr^{-1}) highlights the importance of land management policies for curbing Hg pollution.

Results and Discussion

Global estimate of deforestation-driven Hg fluxes. In quantifying changes to Hg fluxes after deforestation, we define the net deforestation emissions as the change in the net terrestrial-atmosphere exchange (emissions minus deposition) over a deforested area. For our global estimate of deforestation-driven emissions, we do not consider immediate biomass burning emissions of Hg due to fire-mediated forest clearing, instead investigating the impact on net Hg fluxes to the atmosphere in the years after the clearing event. The major impacts to Hg fluxes

arise through enhanced soil Hg^0 emissions and decreased Hg^0 dry deposition, which can continue many years after the initial deforestation event (17, 31). Using perturbation simulations in GEOS-Chem for 8 global land regions, we calculated regional emission factors (EFs) representing net fluxes to the atmosphere per unit deforested area (in units Mg Hg m^{-2} yr^{-1}). The calculated EFs are on the order of 10^{-6} to 10^{-4} Mg Hg m^{-2} yr^{-1} depending on the region (Fig. S4; Table S3), with the Amazon rainforest showing the highest EF (7×10^{-5} Mg Hg m^{-2} yr^{-1}; CI: 4×10^{-5} to 2×10^{-4} Mg Hg m^{-2} yr^{-1}). This is to be expected from litterfall and throughfall measurements in the Amazon, which show some of the highest levels of Hg^0 vegetation uptake observed globally (13), as well as Hg^0 soil flux measurements from deforested areas in the Amazon, which show higher levels of emissions compared to deforested North American soils (17). We compiled available estimates of deforestation EFs from previous observational studies (17, 20, 24, 31–47) and compare these to our modeled values (Fig. S4). Our EFs overlap with available factors derived from observations, for the regions where data are available.

We multiply the regional EFs by the deforested area from the CMIP6 Land-Use Harmonization (LUH2) dataset (48) to calculate the net Hg fluxes to the atmosphere from deforestation. Given the uncertain timescale for recovery in Hg sink capacity after deforestation, we assume that a deforested area has constant annual emissions over a considered time horizon. Previous LULCC studies for carbon suggest that forests recover their original biomass within 75 years after deforestation (49), so we employed time horizons between 15–60 years (Fig. S7) to calculate 2015 deforestation-driven emissions. In Fig. 1a, we present country-level deforestation emissions based on a 45-year time horizon (emissions released from areas deforested between 1970 and 2014). Net emissions occurring in 2015 considering this 45-year deforestation time horizon are 217 Mg yr^{-1} globally (CI: 134–1650 Mg yr^{-1}). Countries with substantial (>10 Mg yr^{-1}) deforestation-driven emissions include Brazil (43 Mg yr^{-1}), Indonesia (35 Mg yr^{-1}), China (16 Mg yr^{-1}), Colombia (14 Mg yr^{-1}), India (13 Mg yr^{-1}), Philippines (11 Mg yr^{-1}), and Myanmar (11 Mg yr^{-1}). To put these emissions into context, Fig. 1b compares the deforestation emissions with 2015 primary anthropogenic emissions inventory from AMAP/UNEP (9, 50). Deforestation Hg emissions are minor (<5%) compared to primary anthropogenic emissions for most countries. However, for 32 countries, all located in the tropics, deforestation emissions are greater than 30% of primary emissions. Deforestation emissions even exceed primary emissions in some countries, including Madagascar (deforestation emissions are 2.4× larger), Paraguay (2.3×), Liberia (2.0×), and Bangladesh (1.8×). For Brazil, which is the fifth highest emitter of primary Hg (9, 50), deforestation emissions (43 Mg yr^{-1}) equate to 60% of the 2015 primary emissions (71 Mg yr^{-1}). Currently, Hg emissions inventories (9) only consider primary anthropogenic emissions (2222 Mg yr^{-1} in 2015), overlooking deforestation as a significant source of anthropogenic Hg to the atmosphere (217 Mg yr^{-1}). The relative importance of deforestation as an anthropogenic driver of Hg pollution could increase over the next decades, with primary anthropogenic emissions of Hg projected to halve to 1020 Mg yr^{-1} by 2035 under Minamata policies and reductions in fossil fuel use (51). Therefore, assessing the potential impacts of land policy scenarios will be crucial for predicting future Hg cycling.

Amazon conservation policy impacts on Hg cycling. The Amazon is one of the regions with the highest Hg fluxes from deforestation (Fig. 1) and policy choices will determine how this evolves in the future. Under historical forest coverage from 2003 (HIST simulation), the Amazon rainforest stands out as a strong global sink of Hg (Fig. 2a), with net input from the atmosphere to the rainforest totaling 332 Mg yr^{-1} (CI: 179–463 Mg yr^{-1}). We study the evolution of the Amazon Hg sink in two deforestation scenarios (27) for 2050: a business-as-usual scenario (BAU), which extrapolates historical deforestation tendencies into the future, and a governance scenario (GOV), which assumes expanded conservation of the rainforest in the future. In the BAU scenario, widespread deforestation, mainly in eastern Amazonia, reduces the net Hg inputs to soils (Fig. 2b). The removed vegetation leads to decreased Hg^0 deposition in the Amazon (change from HIST: -105 Mg yr^{-1}; CI: -53 to -152 Mg yr^{-1}) and enhanced Hg^0 emissions from soils newly exposed to light (+35 Mg yr^{-1} ; CI: 28–275 Mg yr^{-1}). For the Amazon policy scenarios, we have also considered the impact that fire-mediated forest clearing (52, 53) has on biomass

183 burning emissions of Hg, which are 15 Mg yr^{-1} (CI: 10–17 Mg yr^{-1}) larger in BAU than HIST. The
184 BAU scenario shows atmospheric Hg^0 concentrations increasing up to 0.3 ng m^{-3} within the
185 Amazon region (Fig. S12); this would be a detectable change in Hg^0, comparable to the 0.5 ng
186 m^{-3} decrease between 1995–2015 in North American Hg^0 observations (54). In the GOV
187 scenario, deforestation is slowed by the conservation measures, leading to smaller perturbations
188 in the dry deposition flux from HIST (-47 Mg yr^{-1} ; CI: -25 to -68 Mg yr^{-1}) and the soil emission flux
189 (+16 Mg yr^{-1}; CI: 12–126 Mg yr^{-1}) (Fig. 2b). Globally, the weakened rainforest sink of Hg yields
190 higher deposition of Hg to oceans compared to the reference simulation (BAU – HIST = +108 Mg
191 yr^{-1}; GOV – HIST = +44 Mg yr^{-1}). Deforestation can be exacerbated through climate feedbacks,
192 which are not considered in these policy scenarios. For example, BAU projects that 40% of the
193 Amazon will be deforested by 2050 (27), which could trigger a tipping point with widespread
194 transition of the rainforest to a savannah biome under diminished regional moisture recycling
195 (55). To evaluate this, we also re-ran an upper limit scenario from our previous work (23) where
196 the entire rainforest is converted to savannah (SAV). In this case, a strong decline in Hg^0 dry
197 deposition (-359 Mg yr^{-1}; CI: -210 to -503 Mg yr^{-1}) and an increase in Hg^0 soil emissions (+89 Mg
198 yr^{-1}; CI: 68 to 652 Mg yr^{-1}) drive enhanced inputs of Hg to the ocean (343 Mg yr^{-1}) (Fig. 2b).

199 This change in the fate of atmospheric Hg (deposition to ocean instead of land) affects both the
200 spatial distribution and bioavailability of Hg pollution. When sequestered in soils, Hg has an
201 estimated residence time on the order of hundreds of years, whereas in the surface ocean Hg is
202 recycled to the atmosphere within months to years (7, 11). Deforestation thus increases the
203 mobility of Hg by transferring Hg from locally-sequestered reservoirs to the global pool. Human
204 health risks are driven by exposure to the more toxic form of the element, MeHg, which is
205 produced through methylation in the environment (2, 56). Deforestation shifts Hg inputs from land
206 to the ocean, where Hg can more readily be methylated and bioaccumulate to dangerous levels
207 in commercial fish. Methylation and bioaccumulation of Hg can also occur in forested soils, but
208 MeHg levels in aquatic ecosystems are generally much higher (overall global ocean average =
209 15%) (57) than in Amazonian soils (1–5%) (32, 58) . In addition, the long length of aquatic food
210 chains leads to high levels of MeHg in commonly consumed fish species at higher trophic levels
211 (e.g., tuna, cod, and swordfish) (56).

212 Deforestation policy substantially impacts the soil mass balance of Hg in the Amazon region,
213 illustrated by our modeling simulations (Fig. 2c) and available field observations (Fig. S3). If
214 agricultural expansion continues as in BAU, the Amazon sink of atmospheric Hg is weakened by
215 153 Mg yr^{-1} (CI: 97–418 Mg yr^{-1}) (Fig. 2c). Under the more moderate GOV scenario, the Amazon
216 Hg sink (272 Mg yr^{-1}; CI: 79–367 Mg yr^{-1}) is better preserved, though still 18% (CI: 14–65%)
217 smaller than HIST. Stricter conservation policies in GOV yield an additional 92 Mg yr^{-1} (CI: 59–
218 234 Mg yr^{-1}) of Hg sequestered in the Amazon compared to BAU. The SAV scenario illustrates
219 that additional climate feedbacks could flip the Amazon from a net Hg sink to a source (+109 Mg
220 yr^{-1}; CI: 13–768 Mg yr^{-1}). These Hg projections parallel recent findings on Amazon carbon cycling,
221 which have demonstrated that climate change and deforestation are turning the Amazon into a
222 CO_2 source (25). In addition to atmosphere-terrestrial exchange fluxes, soil erosion of Hg can
223 also be altered due to deforestation. We applied a soil erosion model GloSEM (59, 60) to
224 evaluate the impact of deforestation on erosion in the Amazon basin (Supplementary Information
225 Section S6). In terms of Hg flux magnitudes, perturbations to erosion are smaller (<15%) than
226 changes to the atmosphere-terrestrial exchange fluxes (Section S6), which is supported by field
227 studies (47). Nevertheless, deforestation also enhances Hg erosion in both scenarios (BAU:
228 +33%; GOV: +14%), accelerating the transfer of terrestrial Hg to aquatic ecosystems.

229 **Quantifying the Hg mitigation potential of reforestation.** Reforestation has been identified as
230 a potential mitigation approach for climate change, by strengthening the terrestrial CO_2 sink (30,
231 61). To investigate the concurrent strengthening of the terrestrial Hg sink and the impacts on Hg
232 cycling, we considered a global reforestation scenario (RFR) based on the Global Reforestation
233 Potential Map (30, 62), which identified areas suitable for reforestation worldwide (i.e., not
234 including croplands or areas where forests are not native). Figure 3 maps the impacts of
235 reforestation on Hg surface-atmosphere exchange, comparing to the reference HIST simulation.

Globally, RFR enhances uptake of Hg on land by 98 Mg yr^{-1} (CI: 64–449 Mg yr^{-1}), thereby reducing Hg deposition to oceans. Reforestation could thus take up approximately 5% of the anthropogenic Hg emission flux (~2200 Mg yr^{-1}) (9). In addition to the targeted benefits for biodiversity and climate change mitigation (30), reforestation could moderately reduce levels of Hg in marine ecosystems, and thus commercial fish. Nevertheless, the magnitude of reforestation impact (5% of primary emissions) illustrates that reforestation is not a substitute for implementing extensive cuts to primary Hg emissions, like in the CO_2 context (29).

Potential reforestation opportunities for Hg are dominated by the Amazon and Atlantic forest regions in South America (71 Mg yr^{-1}, 72% of total land sink impact) (Fig. 3). The potential reforestation impact on atmospheric fluxes in Northern extratropical areas alone (-29 Mg yr^{-1}) cannot compensate for increased deforestation Hg emissions in the Amazon (BAU: +153 Mg yr^{-1}; GOV: +61 Mg yr^{-1}). Overall, more information would be needed to compare the potentials of reforestation and conservation policies on a global scale, as the deforestation policy scenarios focused only on a specific region (the Amazon); future research could study conservation impacts in other tropical regions with high Hg deforestation emissions (Fig. 1) (e.g., in Africa and Southeast Asia).

Implications for global Hg policy and caveats. Land use policy has been largely unexplored as a lever to mitigate Hg pollution. On the global scale, the estimated deforestation-driven Hg emissions in 2015 (217 Mg yr^{-1}; CI: 134–1650 Mg yr^{-1}) correspond to 10% of the global primary anthropogenic emissions (9) (2222 Mg yr^{-1}) (Fig. 4a). Therefore, though cutting primary anthropogenic emissions remains a priority, deforestation fluxes should not be overlooked in assessments of Hg pollution, especially for countries in the tropics (Fig. 1b). The potential of Amazon conservation and global reforestation to reduce net Hg emissions in the future is substantial compared to previously quantified policies aimed at tackling primary anthropogenic emissions (Fig. 4b). Potential emissions reductions from Amazon conservation (92 Mg yr^{-1}) and global reforestation (98 Mg yr^{-1}) are within the range of impacts of past policy and future policy scenarios aimed at reducing Hg from specific anthropogenic sources or due to national climate and air pollution policies (5–262 Mg yr^{-1}) (63–68). Emissions reductions from land use policies are different from primary emissions reductions in that their efficacy depends on whether the storage of Hg in soils is over a long-term period. Similar to CO_2, the potential benefits of enhanced Hg uptake on land can be reversed by human or natural disturbances, e.g., by climate change increasing the frequency of wildfires — which re-emit Hg and carbon from terrestrial ecosystems — and droughts — which reduce Hg and CO_2 uptake by plants (30, 69). Thus, mitigation of Hg pollution by conserving and increasing forest area can only be realized with concurrent efforts to sustainably manage land areas and preventing severe climate change. The potential of sustainable land use to mitigate Hg pollution could enable collaborations between the Minamata Convention and other global policy efforts to reduce deforestation, e.g., the 2021 Glasgow Declaration (70).

The current work provides an initial assessment of the global emissions of Hg from deforestation, which can spur future investigation into the impact of LULCC on Hg. Other LULCC processes (e.g., wood harvest and agricultural practices) may also affect Hg fluxes but have not been considered within this study. As well, due to the early stage of Hg research, we do not yet have the same level of information for Hg that is commonly included in LULCC assessments for carbon, including temporal information on the release of Hg from soils and Hg uptake rates during regrowth of vegetation (22). There is a lack of measurements in relevant regions (e.g., Afrotropic and Indomalayan) to constrain the response of Hg fluxes to deforestation, contributing uncertainty to this work. Further development of terrestrial Hg cycles and LULCC processes within Earth system models (71) will be vital to investigate the evolution of the Hg land sink over time and the effect on environmental Hg risks. Ultimately, mitigation of global Hg pollution depends not only on reducing primary anthropogenic emissions, but also reducing anthropogenic activities like deforestation that re-mobilize legacy Hg.

Materials and Methods

Atmospheric Hg model (GEOS-Chem) description. In this study, we use GEOS-Chem v12.8.1 with Hg^0 dry deposition updates from Feinberg et al. (23). The global model is run at 2.0° × 2.5° horizontal resolution and 47 vertical layers up to 80 km altitude. The model tracks emissions, transport, chemistry, and deposition of Hg in three chemical tracers: elemental mercury (Hg^0), oxidized mercury (Hg^{II}), and particulate-bound mercury (Hg^P). Atmospheric transport of Hg species is based on MERRA-2 reanalysis meteorological data (72). The Hg chemical mechanism assumes that Br is the primary Hg oxidant and uses offline monthly maps of previously-calculated oxidant concentrations to drive chemistry (73). The aqueous photoreduction rate of Hg^{II} to Hg^0 is parametrized as a function of the organic aerosol concentration and the NO_2 photolysis rate (73).

The wet removal of oxidized Hg (Hg^{II} and Hg^P) from the atmosphere is calculated in online parametrizations considering large-scale and convective scavenging of gas and particulate species (74). Dry deposition in GEOS-Chem applies a resistance-based approach (75), which determines the dry deposition velocities depending on meteorology (e.g., temperature and windspeed), land surface parameters (e.g., land type and leaf area index, LAI), and compound-specific parameters (biological reactivity, f_0, and solubility, H^*). For Hg^0, f_0 is set to 0.2 within the Amazon rainforest and 3×10^{-5} elsewhere, which was found to yield the best agreement with measurements of Hg^0 vegetation uptake (23). The solubility of Hg^0 is low (H^* = 0.11 M atm^{-1}), whereas gaseous Hg^{II} is assumed to be highly soluble ($H^* = 10^{14}$ M atm^{-1}) and biologically unreactive (f_0 = 0). Dry deposition of Hg^P is determined according to the aerosol deposition parameterization in GEOS-Chem (76). Dry deposition is calculated separately over each land type within a grid cell (e.g., rainforest, grassland, cropland, etc.) and then an overall area-weighted average is calculated for the grid cell. GEOS-Chem accounts for 73 land types based on the Gibbs (77) land cover product. The LAI data for this study is taken from a reprocessed version of the Moderate Resolution Imaging Spectroradiometer (MODIS) satellite product (78).

Anthropogenic Hg emissions follow AMAP/UNEP estimates (50) for 2015. Biomass burning emissions are taken from the Global Fire Emissions Database (GFED) v4.1s (79). We use fixed concentrations of Hg^0 in the surface ocean based on the MITgcm 3-D ocean model (73) to calculate the Hg^0 air-sea exchange (80). We adopted a new formulation (81) for the soil Hg^0 emissions parametrization (Supplementary Information, Section S1):

$$E_{\text{soil}} = aC^b R_g^c \quad (1)$$

where E_{soil} is the Hg^0 emissions from soil (units ng m^{-2} h^{-1}), C is the concentration of Hg in soils, R_g is solar radiation flux at the ground, and *a, b,* and *c,* are coefficients (set to 71, 2.5, and 0.76, respectively). We have tuned the coefficients of this parametrization to match available soil emissions measurements from the Amazon and extratropics (Section S2). The soil concentration map of Hg (C) was calculated using the method of Selin et al. (82), deriving the spatial distribution of soil concentrations by first assuming a steady state balance between land emissions and deposition in the preindustrial and subsequently increasing soil concentrations according to the distribution of anthropogenic Hg deposition. As in Selin et al. (82), the solar radiation at ground (R_g) is determined by considering attenuation of the solar radiation flux (R_S) by shading from the overhead canopy, parametrized by the LAI:

$$R_g = R_S \exp\left(-\frac{\alpha \text{LAI}}{\cos\theta}\right) \quad (2)$$

where α = 0.5, assuming extinction from a random angular distribution of leaves (83), and θ is the solar zenith angle. We have also updated GEOS-Chem to calculate soil emissions at the sub-grid scale for each land use category contained within the grid cell.

Reference (HIST) simulation. We ran a GEOS-Chem simulation for the land cover and LAI conditions of the year 2003 (HIST simulation), the baseline year in the Amazon deforestation policy scenarios (27). To highlight the role of land cover changes alone, we keep meteorological conditions constant by running all simulations with meteorology for 2014–2015. We consider the first year as spinup to equilibrate the new land cover conditions, and analyze simulation differences for the meteorological year 2015.

Estimating historical global deforestation-driven Hg emissions. We calculate regional emissions factors (EFs) for deforestation through conducting perturbation experiments in GEOS-Chem. We distinguish emission factors for the following regions based on biogeographic realms (84) or specific Hg-relevant characteristics: Palearctic, Nearctic, Afrotropic, Neotropic, Australasia & Oceania, Indomalaya, China, and the Amazon rainforest (mapped in Fig. S6). For each region, we conduct a simulation where we perturb the land cover in grid cells that experience deforestation during 2000–2014 in the 0.25° × 0.25° resolution CMIP6 Land-Use Harmonization (LUH2) dataset (48). For these grid cells, we replace forest land cover with the most common agricultural land cover relevant to the region: “Crops and Town” (Afrotropic, Indomalaya, Palearctic, Australasia & Oceania, and China), “Corns and Beans Croplands” (Neotropic and Nearctic), and “Fields and Woody Savannah” (Amazon). For the new agricultural areas, the LAI is set to the average annual cycle for the existing agricultural grid cells within the region. We run 8 deforestation (DFR) simulations (1 for each region) over 2014–2015, comparing year 2015 fluxes to the HIST simulation. To calculate the net emissions factor (EF) from deforestation, we calculate changes to the land-air exchange over the deforested grid cells:

$$\mathrm{EF} = \frac{(E_{\mathrm{DFR}} - D_{\mathrm{DFR}}) - (E_{\mathrm{HIST}} - D_{\mathrm{HIST}})}{A_{\mathrm{DFR}}} \quad (4)$$

where *E* refers to Hg emissions, *D* refers to Hg deposition, and *A* refers to the area that is deforested in the simulation. The emissions factor represents the net emissions of Hg released by a deforested area annually, in units Mg m^{-2} yr^{-1}. The assumption of linearity of the net emissions to deforested area holds over simulations conducted in the Amazon with differing spatial distributions of deforestation (Fig. S5), supporting an emissions factor approach to deforestation. We compared calculated emissions factors with existing estimates from observational and modeling studies (17, 20, 24, 31–47), finding overlapping agreement for regions where observational evidence is available (Fig. S4).

We apply the regional emissions factor to historical land use data from the LUH2 dataset to calculate emissions from deforestation. We define gross deforested areas from the LUH2 dataset by summing the areas with transitions from primary or secondary forest to a non-forest land type. This approach does not consider LULCC fluxes due to harvesting of a forest without complete deforestation or the regrowth of vegetation after clearing, due to a lack of corresponding observations for Hg to constrain these parameters. Likewise, the emissions factors are assumed to be constant over time, so a deforested area continues to have the same annual emissions over the considered time horizon. In reality, deforested areas could have a recovery timescale as vegetation regrows, which is accounted for in carbon LULCC fluxes (49); for Hg, the response timescales during regrowth are largely unknown. To account for these uncertainties, we produce global and country-level estimates of Hg emissions in 2015 due to deforestation by summing deforestation over different time horizons: 15 years (2000–2014), 30 years (1985–2014), 45 years (1970–2014), and 60 years (1955–2014). We present the 45-year (1970–2014) accumulated results in the main text, with the others presented in Fig. S7.

Future Amazon deforestation scenarios. We employ deforestation scenarios from Soares-Filho et al. (27), who developed a model for predicting the extent of deforestation within the Amazon based on environmental policies and highway construction. They presented two scenarios for 2050, encompassing a range of future deforestation trajectories. In the Business as Usual (BAU) scenario, recent deforestation trends continue into the future, assuming that compliance with conservation laws remains low and no new areas will be protected. On the other

hand, the Governance (GOV) scenario assumes the expansion of environmental legislation and increased enforcement of protected areas will lead to a reduction in the deforestation rate. Compared to the Amazon forest area in 2003 (5.3 million km^2), in 2050 the BAU scenario projects 3.2 million km^2 remaining and GOV projects 4.5 million km^2 remaining (27). We focus our analysis on comparing the forest coverage in the years 2003 and 2050.

We translated these scenarios into required inputs for the calculations in GEOS-Chem (spatially gridded land use categories, LAI, and biomass burning emissions). The Soares-Filho et al. (27) dataset assigns 1 km^2 pixels within the Amazon basin as being forested, deforested, or agricultural areas for every year between 2003 and 2050. We regridded these annual datasets to 0.25° × 0.25° resolution, the native resolution of land use and LAI maps in GEOS-Chem. We calculated the relative change in forested area in the scenarios for every 0.25° × 0.25° grid cell. The rainforest land use category in deforested grid cells is correspondingly reduced by this factor, with the lost land area added to the land use category for "Fields and Woody Savanna". The LAI annual cycle for existing Fields and Woody Savanna grid cells within the Amazon basin was spatially averaged over 2003 and assigned to the deforested areas. Annual average LAI maps for the Amazon scenarios used in GEOS-Chem are shown in Fig. S10. For these simulations, we assume that conversion of forest to agricultural land within the Amazon is fire-mediated (52). Gridded biomass burning emissions are calculated by multiplying the newly deforested areas for each year by mean fire Hg emissions (380 μg m^{-2} yr^{-1}) from two observational studies in the Amazon (18, 85). An additional 50% of the emissions (190 μg m^{-2} yr^{-1}) are released to the atmosphere within the first year as post-burn Hg^0 emissions from soils (17). To account for seasonal differences in meteorology and realistic timing for forest clearing and burning (52), we assumed that deforestation occurs at the start of June and deforestation biomass burning emissions occur in August and September .

The BAU and GOV scenarios do not account for any land-climate feedbacks (27), wherein deforestation of the rainforest can lead to reduced moisture recycling and widespread *savannization* (conversion of rainforest to savanna) (55). As an upper bound for this process, we consider an extreme scenario (SAV) where the Amazon rainforest is fully converted to savanna (86). The impact of this scenario on Hg^0 deposition was previously quantified (23), but here we reran the SAV simulation in GEOS-Chem to account for updates in the soil Hg^0 emissions parametrization. In the analysis of results, we calculate fluxes for the Amazon region, averaging over the area covered by the Soares-Filho et al. (27) deforestation projections (shown in Fig. S9).

Potential reforestation scenarios. We apply a reforestation scenario (RFR) in GEOS-Chem based on the Global Reforestation Potential map (30, 62), which considers the binary potential of every 1 km^2 grid cell to be converted from non-forest (<25% tree cover in 2000–2009) to forest (>25% tree cover). The reforestation potential dataset does not include areas that are native non-forest land cover types (e.g., grasslands) or cropland areas. We regridded the reforestation potential to 0.25° × 0.25° resolution. For every grid cell where reforestation can occur, we identify the corresponding biome in the Ecoregions2017 dataset (84) to determine the type of native forest vegetation that would occur. If the corresponding biome of the grid cell is not a forest (e.g., coastal grid cells), we identify the most common forest type in the 8 neighboring grid cells. The added forest is assumed to have a LAI annual cycle equal to the 2003 spatial average for all grid cells in the corresponding biome and biogeographic realm (LAI_{biome}). For grid cells that are not a forest land type in 2003, we convert the reforested area fraction (f_{rfr}) from the original land type to the new forest land type. We only reforest grid cells in the case where LAI_{biome} is larger than the original land type LAI (LAI_{old}). Since the land map used in GEOS-Chem is at coarser resolution (0.25° × 0.25°) than the reforestation potential dataset (1 km × 1 km), the reforested grid cell may already be a forest land type in GEOS-Chem. In this case, we assume that the grid cell LAI (LAI_{new}) will become denser due to the new reforested area:

$$\mathrm{LAI}_{\mathrm{new}} = \mathrm{LAI}_{\mathrm{old}} + f_{\mathrm{rfr}} \cdot \mathrm{LAI}_{\mathrm{biome}} \quad (3)$$

The resultant average LAI map in the RFR scenario is shown in Fig. S11.

Uncertainty analysis. Due to the computational expense of conducting uncertainty analyses in the online GEOS-Chem model, we employ offline Python-based models for Hg^0 dry deposition and soil Hg^0 emissions to calculate uncertainties in the terrestrial-atmosphere Hg fluxes. The Hg^0 dry deposition and soil emissions changes contribute the overwhelming majority (>98%) of the flux response to deforestation. We consider the contributions of deposition parameters, soil emission parametrizations, the assumption for LAI for replaced land types, and biomass burning emission factors (for the Amazon simulations) to the overall uncertainty in fluxes. Uncertainty bounds of these parameters are tabulated in Table S4. We sample 100 parameter combinations using Latin Hypercube sampling (87). The offline models were run for the year 2015 using monthly average diurnal cycles (12 × 24 h = 288 timesteps) of meteorological parameters, land surface parameters, and Hg^0 concentration fields. At this time resolution, the offline models show sufficient accuracy to assess parameter uncertainties, with maximum errors compared to online predictions of 1% for annual mean soil emissions and 5% for Hg^0 deposition. We conducted 100 simulations in the offline emissions and deposition models for each studied scenario, calculating 95% confidence intervals from the 2.5th and 97.5th percentile values in the offline calculated fluxes.

Acknowledgments

This work was funded by the Swiss National Science Foundation through an Early Postdoc.Mobility grant to A.F. (P2EZP2_195424) and an Ambizione grant to M.J. (PZ00P2_174101), a grant (#1924148) from the US National Science Foundation to N.E.S., and an Academic Transition Grant from Eawag to J.B. We thank Ronny Meier and Michael Windisch for assistance in processing the reforestation potential dataset. We thank Luiz D. Lacerda for sharing Hg data from Brazil. We acknowledge researchers involved in conducting field studies measuring the impact of deforestation on Hg fluxes in the Amazon and elsewhere.

Code and Data Availability

Model code, analysis scripts, and simulation data supporting the results of this study are published in Zenodo (https://doi.org/10.5281/zenodo.7957157) under a CC BY 4.0 license (https://creativecommons.org/licenses/by/4.0/).

References

1. M. C. Sheehan, *et al.*, Global methylmercury exposure from seafood consumption and risk of developmental neurotoxicity: a systematic review. *Bull. World Health Organ.* **92**, 254-269F (2014).
2. Y. Zhang, *et al.*, Global health effects of future atmospheric mercury emissions. *Nat Commun* **12**, 3035 (2021).
3. M. Bellanger, *et al.*, Economic benefits of methylmercury exposure control in Europe: Monetary value of neurotoxicity prevention. *Environ Health* **12**, 3 (2013).
4. P. M. Outridge, R. P. Mason, F. Wang, S. Guerrero, L. E. Heimbürger-Boavida, Updated Global and Oceanic Mercury Budgets for the United Nations Global Mercury Assessment 2018. *Environ. Sci. Technol.*, acs.est.8b01246 (2018).
5. V. Shah, *et al.*, Improved Mechanistic Model of the Atmospheric Redox Chemistry of Mercury. *Environ. Sci. Technol.* **55**, 14445–14456 (2021).
6. UNTC, Minamata Convention on Mercury (2013). https://treaties.un.org/Pages/ViewDetails.aspx?src=TREATY&mtdsg_no=XXVII-17&chapter=27
7. H. M. Amos, D. J. Jacob, D. G. Streets, E. M. Sunderland, Legacy impacts of all-time anthropogenic emissions on the global mercury cycle. *Global Biogeochem. Cycles* **27**, 410–421 (2013).
8. J. Zhou, D. Obrist, A. Dastoor, M. Jiskra, A. Ryjkov, Vegetation uptake of mercury and impacts on global cycling. *Nat. Rev. Earth Environ.* **2**, 269–284 (2021).

9. UNEP, *Global Mercury Assessment 2018* (UN Environment Programme, Chemicals and Health Branch. Geneva, Switzerland, 2019).
10. K. Schaefer, *et al.*, Potential impacts of mercury released from thawing permafrost. *Nat Commun* **11**, 4650 (2020).
11. N. V. Smith-Downey, E. M. Sunderland, D. J. Jacob, Anthropogenic impacts on global storage and emissions of mercury from terrestrial soils: Insights from a new global model. *J. Geophys. Res.* **115**, G03008 (2010).
12. M. Jiskra, *et al.*, A vegetation control on seasonal variations in global atmospheric mercury concentrations. *Nature Geosci* **11**, 244–250 (2018).
13. A. H. Fostier, J. J. Melendez-Perez, L. Richter, Litter mercury deposition in the Amazonian rainforest. *Environ. Pollut.* **206**, 605–610 (2015).
14. IPCC, *Climate Change and Land: an IPCC special report on climate change, desertification, land degradation, sustainable land management, food security, and greenhouse gas fluxes in terrestrial ecosystems*, P. R. Shukla, *et al.*, Eds. (2019).
15. H. Zhang, C. D. Holmes, S. Wu, Impacts of changes in climate, land use and land cover on atmospheric mercury. *Atmos. Environ.* **141**, 230–244 (2016).
16. UNFCC, The Paris Agreement (2015). https://unfccc.int/process-and-meetings/the-paris-agreement/the-paris-agreement
17. A. Carpi, A. H. Fostier, O. R. Orta, J. C. dos Santos, M. Gittings, Gaseous mercury emissions from soil following forest loss and land use changes: Field experiments in the United States and Brazil. *Atmos. Environ.* **96**, 423–429 (2014).
18. J. J. Melendez-Perez, *et al.*, Soil and biomass mercury emissions during a prescribed fire in the Amazonian rain forest. *Atmospheric Environment* **96**, 415–422 (2014).
19. M. Roulet, *et al.*, Effects of Recent Human Colonization on the Presence of Mercury in Amazonian Ecosystems. *Water Air Soil Pollut.* **112**, 297–313 (1999).
20. A. H. Fostier, *et al.*, Mercury fluxes in a natural forested Amazonian catchment (Serra do Navio, Amapá State, Brazil). *Sci. Total Environ.* **260**, 201–211 (2000).
21. R. Adler Miserendino, *et al.*, Mercury Pollution in Amapá, Brazil: Mercury Amalgamation in Artisanal and Small-Scale Gold Mining or Land-Cover and Land-Use Changes? *ACS Earth Space Chem.* **2**, 441–450 (2018).
22. W. A. Obermeier, *et al.*, Modelled land use and land cover change emissions – a spatio-temporal comparison of different approaches. *Earth Syst. Dynam.* **12**, 635–670 (2021).
23. A. Feinberg, T. Dlamini, M. Jiskra, V. Shah, N. E. Selin, Evaluating atmospheric mercury (Hg) uptake by vegetation in a chemistry-transport model. *Environ. Sci.: Processes Impacts* **24**, 1303–1318 (2022).
24. X. Wang, *et al.*, Emission-dominated gas exchange of elemental mercury vapor over natural surfaces in China. *Atmos. Chem. Phys.* **16**, 11125–11143 (2016).
25. L. V. Gatti, *et al.*, Amazonia as a carbon source linked to deforestation and climate change. *Nature* **595**, 388–393 (2021).
26. A. Tyukavina, *et al.*, Types and rates of forest disturbance in Brazilian Legal Amazon, 2000–2013. *Sci. Adv.* **3**, e1601047 (2017).
27. B. S. Soares-Filho, *et al.*, Modelling conservation in the Amazon basin. *Nature* **440**, 520–523 (2006).
28. IPCC, “Summary for Policymakers” in *Climate Change 2022: Mitigation of Climate Change. Contribution of Working Group III to the Sixth Assessment Report of the Intergovernmental Panel on Climate Change*, ([P.R. Shukla, J. Skea, R. Slade, A. Al Khourdajie, R. van Diemen, D. McCollum, M. Pathak, S. Some, P. Vyas, R. Fradera, M. Belkacemi, A. Hasija, G. Lisboa, S. Luz, J. Malley, (eds.)]. Cambridge University Press, Cambridge, UK and New York, NY, USA).
29. K. D. Holl, P. H. S. Brancalion, Tree planting is not a simple solution. *Science* **368**, 580–581 (2020).
30. B. W. Griscom, *et al.*, Natural climate solutions. *Proc. Natl. Acad. Sci. U.S.A.* **114**, 11645–11650 (2017).

31. R. L. Gamby, C. R. Hammerschmidt, D. M. Costello, C. H. Lamborg, J. R. Runkle, Deforestation and cultivation mobilize mercury from topsoil. *Science of The Total Environment* **532**, 467–473 (2015).
32. J. R. Gerson, *et al.*, Amazon forests capture high levels of atmospheric mercury pollution from artisanal gold mining. *Nat Commun* **13**, 559 (2022).
33. M. D. Almeida, L. D. Lacerda, W. R. Bastos, J. C. Herrmann, Mercury loss from soils following conversion from forest to pasture in Rondônia, Western Amazon, Brazil. *Environmental Pollution* **137**, 179–186 (2005).
34. M. D. Almeida, R. V. Marins, H. H. M. Paraquetti, W. R. Bastos, L. D. Lacerda, Mercury degassing from forested and open field soils in Rondônia, Western Amazon, Brazil. *Chemosphere* **77**, 60–66 (2009).
35. L. D. Lacerda, M. de Souza, M. G. Ribeiro, The effects of land use change on mercury distribution in soils of Alta Floresta, Southern Amazon. *Environmental Pollution* **129**, 247–255 (2004).
36. A. Béliveau, M. Lucotte, R. Davidson, L. O. do Canto Lopes, S. Paquet, Early Hg mobility in cultivated tropical soils one year after slash-and-burn of the primary forest, in the Brazilian Amazon. *Science of The Total Environment* **407**, 4480–4489 (2009).
37. A. Béliveau, *et al.*, Reduction of soil erosion and mercury losses in agroforestry systems compared to forests and cultivated fields in the Brazilian Amazon. *Journal of Environmental Management* **203**, 522–532 (2017).
38. C. Patry, R. Davidson, M. Lucotte, A. Béliveau, Impact of forested fallows on fertility and mercury content in soils of the Tapajós River region, Brazilian Amazon. *Science of The Total Environment* **458–460**, 228–237 (2013).
39. I. Comte, *et al.*, Impacts of Land Uses on Mercury Retention in Long-Time Cultivated Soils, Brazilian Amazon. *Water Air Soil Pollut* **224**, 1515 (2013).
40. G. Magarelli, A. Fostier, Influence of deforestation on the mercury air/soil exchange in the Negro River Basin, Amazon. *Atmos. Environ.* **39**, 7518–7528 (2005).
41. N. Mainville, *et al.*, Decrease of soil fertility and release of mercury following deforestation in the Andean Amazon, Napo River Valley, Ecuador. *Science of The Total Environment* **368**, 88–98 (2006).
42. M. Roulet, *et al.*, The geochemistry of mercury in central Amazonian soils developed on the Alter-do-Chão formation of the lower Tapajós River Valley, Pará state, Brazil. *Science of The Total Environment* **223**, 1–24 (1998).
43. J. C. Wasserman, R. C. Campos, S. de S. Hacon, R. A. Farias, S. M. Caires, Mercury in soils and sediments from gold mining liabilities in Southern Amazonia. *Quím. Nova* **30** (2007).
44. P. S. Homann, R. L. Darbyshire, B. T. Bormann, B. A. Morrissette, Forest Structure Affects Soil Mercury Losses in the Presence and Absence of Wildfire. *Environ. Sci. Technol.* **49**, 12714–12722 (2015).
45. M. Mazur, *et al.*, Gaseous mercury fluxes from forest soils in response to forest harvesting intensity: A field manipulation experiment. *Science of The Total Environment* **496**, 678–687 (2014).
46. M. Ma, D. Wang, R. Sun, Y. Shen, L. Huang, Gaseous mercury emissions from subtropical forested and open field soils in a national nature reserve, southwest China. *Atmospheric Environment* **64**, 116–123 (2013).
47. C. S. Eckley, C. Eagles-Smith, M. T. Tate, D. P. Krabbenhoft, Surface-air mercury fluxes and a watershed mass balance in forested and harvested catchments. *Environmental Pollution* **277**, 116869 (2021).
48. G. C. Hurtt, *et al.*, Harmonization of global land use change and management for the period 850–2100 (LUH2) for CMIP6. *Geosci. Model Dev.* **13**, 5425–5464 (2020).
49. N. Ramankutty, *et al.*, Challenges to estimating carbon emissions from tropical deforestation. *Global Change Biol* **13**, 51–66 (2007).
50. F. Steenhuisen, S. J. Wilson, Development and application of an updated geospatial distribution model for gridding 2015 global mercury emissions. *Atmos. Environ.* **211**, 138–150 (2019).

51. J. M. Pacyna, *et al.*, Current and future levels of mercury atmospheric pollution on a global scale. *Atmos. Chem. Phys.* **16**, 12495–12511 (2016).
52. M. E. Crespo-Lopez, *et al.*, Mercury: What can we learn from the Amazon? *Environment International* **146**, 106223 (2021).
53. J. A. Fisher, *et al.*, A synthesis of mercury research in the Southern Hemisphere, part 2: Anthropogenic perturbations. *Ambio* **52**, 918–937 (2023).
54. Y. Zhang, *et al.*, Observed decrease in atmospheric mercury explained by global decline in anthropogenic emissions. *Proc. Natl. Acad. Sci. U.S.A.* **113**, 526–531 (2016).
55. T. E. Lovejoy, C. Nobre, Amazon Tipping Point. *Sci. Adv.* **4**, eaat2340 (2018).
56. A. T. Schartup, *et al.*, Climate change and overfishing increase neurotoxicant in marine predators. *Nature* **572**, 648–650 (2019).
57. Y. Zhang, A. L. Soerensen, A. T. Schartup, E. M. Sunderland, A Global Model for Methylmercury Formation and Uptake at the Base of Marine Food Webs. *Global Biogeochem. Cycles* **34** (2020).
58. M. Roulet, Guimarães, J.R.D, Lucotte, M, Methylmercury production and accumulation in sediments and soils of an Amazonian floodplain – effect of seasonal inundation. *Water, Air, and Soil Pollution* **128**, 41–60 (2001).
59. P. Borrelli, *et al.*, Land use and climate change impacts on global soil erosion by water (2015-2070). *Proc. Natl. Acad. Sci. U.S.A.* **117**, 21994–22001 (2020).
60. P. Borrelli, *et al.*, An assessment of the global impact of 21st century land use change on soil erosion. *Nat Commun* **8**, 2013 (2017).
61. J.-F. Bastin, *et al.*, The global tree restoration potential. *Science* **365**, 76–79 (2019).
62. B. W. Griscom, *et al.*, "Global Reforestation Potential Map" (Zenodo, 2017). https://doi.org/10.5281/zenodo.883444
63. K. Liu, *et al.*, Measure-Specific Effectiveness of Air Pollution Control on China's Atmospheric Mercury Concentration and Deposition during 2013–2017. *Environ. Sci. Technol.* **53**, 8938–8946 (2019).
64. EPA, "National Emission Standards for Hazardous Air Pollutants: Coal- and Oil-Fired Electric Utility Steam Generating Units—Reconsideration of Supplemental Finding and Residual Risk and Technology Review" (2019). https://www.govinfo.gov/content/pkg/FR-2019-02-07/pdf/2019-00936.pdf
65. Environment and Climate Change Canada, "Evaluation of the effectiveness of risk management measures for mercury" (2020). https://www.canada.ca/en/environment-climate-change/services/management-toxic-substances/evaluation-effectiveness-risk-management-measures-mercury.html
66. D. E. Bruno, *et al.*, Reducing Mercury Emission Uncertainty from Artisanal and Small-Scale Gold Mining Using Bootstrap Confidence Intervals: An Assessment of Emission Reduction Scenarios. *Atmosphere* **14**, 62 (2022).
67. K. M. Mulvaney, *et al.*, Mercury Benefits of Climate Policy in China: Addressing the Paris Agreement and the Minamata Convention Simultaneously. *Environ. Sci. Technol.* **54**, 1326–1335 (2020).
68. P. Rafaj, J. Cofala, J. Kuenen, A. Wyrwa, J. Zyśk, Benefits of European Climate Policies for Mercury Air Pollution. *Atmosphere* **5**, 45–59 (2014).
69. L. Wohlgemuth, *et al.*, Physiological and climate controls on foliar mercury uptake by European tree species. *Biogeosciences* **19**, 1335–1353 (2022).
70. COP26, "Glasgow Leaders' Declaration on Forests and Land Use" (2021). https://ukcop26.org/glasgow-leaders-declaration-on-forests-and-land-use/
71. T. Yuan, *et al.*, Buffering effect of global vegetation on the air-land exchange of mercury: Insights from a novel terrestrial mercury model based on CESM2-CLM5. *Environment International* **174**, 107904 (2023).
72. R. Gelaro, *et al.*, The Modern-Era Retrospective Analysis for Research and Applications, Version 2 (MERRA-2). *J. Clim.* **30**, 5419–5454 (2017).
73. H. M. Horowitz, *et al.*, A new mechanism for atmospheric mercury redox chemistry: implications for the global mercury budget. *Atmos. Chem. Phys.* **17**, 6353–6371 (2017).

74. H. M. Amos, *et al.*, Gas-particle partitioning of atmospheric Hg(II) and its effect on global mercury deposition. *Atmos. Chem. Phys.* **12**, 591–603 (2012).
75. Y. Wang, D. J. Jacob, J. A. Logan, Global simulation of tropospheric O_3-NO_x-hydrocarbon chemistry: 1. Model formulation. *J. Geophys. Res.* **103**, 10713–10725 (1998).
76. J. A. Fisher, *et al.*, Sources, distribution, and acidity of sulfate–ammonium aerosol in the Arctic in winter–spring. *Atmos. Environ.* **45**, 7301–7318 (2011).
77. H. K. Gibbs, Olson's Major World Ecosystem Complexes Ranked by Carbon in Live Vegetation: An Updated Database Using the GLC2000 Land Cover Product (NDP-017b). https://www.osti.gov/biblio/1389498, 2006 (2006).
78. H. Yuan, Y. Dai, Z. Xiao, D. Ji, W. Shangguan, Reprocessing the MODIS Leaf Area Index products for land surface and climate modelling. *Remote Sens. Environ.* **115**, 1171–1187 (2011).
79. G. R. van der Werf, *et al.*, Global fire emissions estimates during 1997–2016. *Earth Syst. Sci. Data* **9**, 697–720 (2017).
80. S. A. Strode, *et al.*, Air-sea exchange in the global mercury cycle. *Global Biogeochem. Cycles* **21**, GB1017 (2007).
81. T. R. Khan, D. Obrist, Y. Agnan, N. E. Selin, J. A. Perlinger, Atmosphere-terrestrial exchange of gaseous elemental mercury: parameterization improvement through direct comparison with measured ecosystem fluxes. *Environ. Sci.: Processes Impacts* **21**, 1699–1712 (2019).
82. N. E. Selin, *et al.*, Global 3-D land-ocean-atmosphere model for mercury: Present-day versus preindustrial cycles and anthropogenic enrichment factors for deposition. *Global Biogeochem. Cycles* **22**, GB2011 (2008).
83. M. M. Verstraete, Radiation transfer in plant canopies: Transmission of direct solar radiation and the role of leaf orientation. *J. Geophys. Res.* **92**, 10985 (1987).
84. E. Dinerstein, *et al.*, An Ecoregion-Based Approach to Protecting Half the Terrestrial Realm. *BioScience* **67**, 534–545 (2017).
85. P. A. M. Michelazzo, A. H. Fostier, G. Magarelli, J. C. Santos, J. A. de Carvalho, Mercury emissions from forest burning in southern Amazon. *Geophys. Res. Lett.* **37**, L09809 (2010).
86. B. F. Alves de Oliveira, M. J. Bottino, P. Nobre, C. A. Nobre, Deforestation and climate change are projected to increase heat stress risk in the Brazilian Amazon. *Commun. Earth Environ.* **2**, 207 (2021).
87. M. D. McKay, R. J. Beckman, W. J. Conover, Comparison of Three Methods for Selecting Values of Input Variables in the Analysis of Output from a Computer Code. *Technometrics* **21**, 239–245 (1979).

686 **Figures**
687

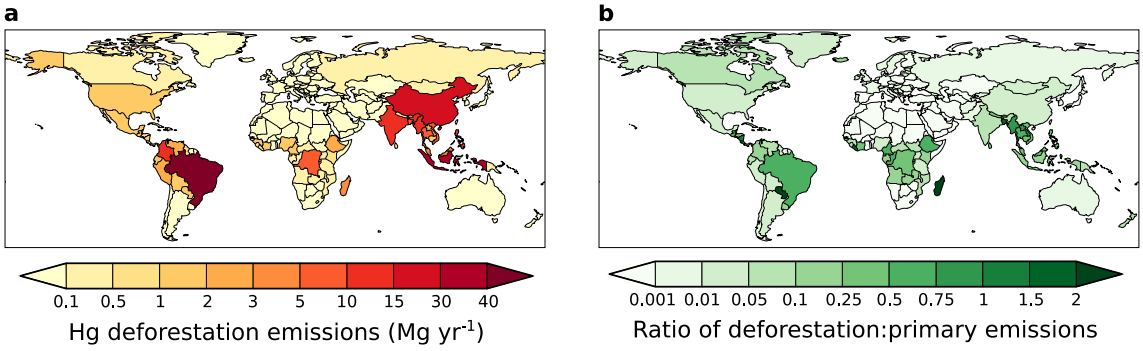

688

689 **Figure 1.** Country-level annual deforestation emissions of Hg in 2015. (*a*) Deforestation-driven
690 net emissions of Hg by country, assuming that deforested areas from the previous 45 years
691 (1970–2014) contribute to emissions. (*b*) Ratio of deforestation emissions to primary
692 anthropogenic emissions (9, 50) by country.

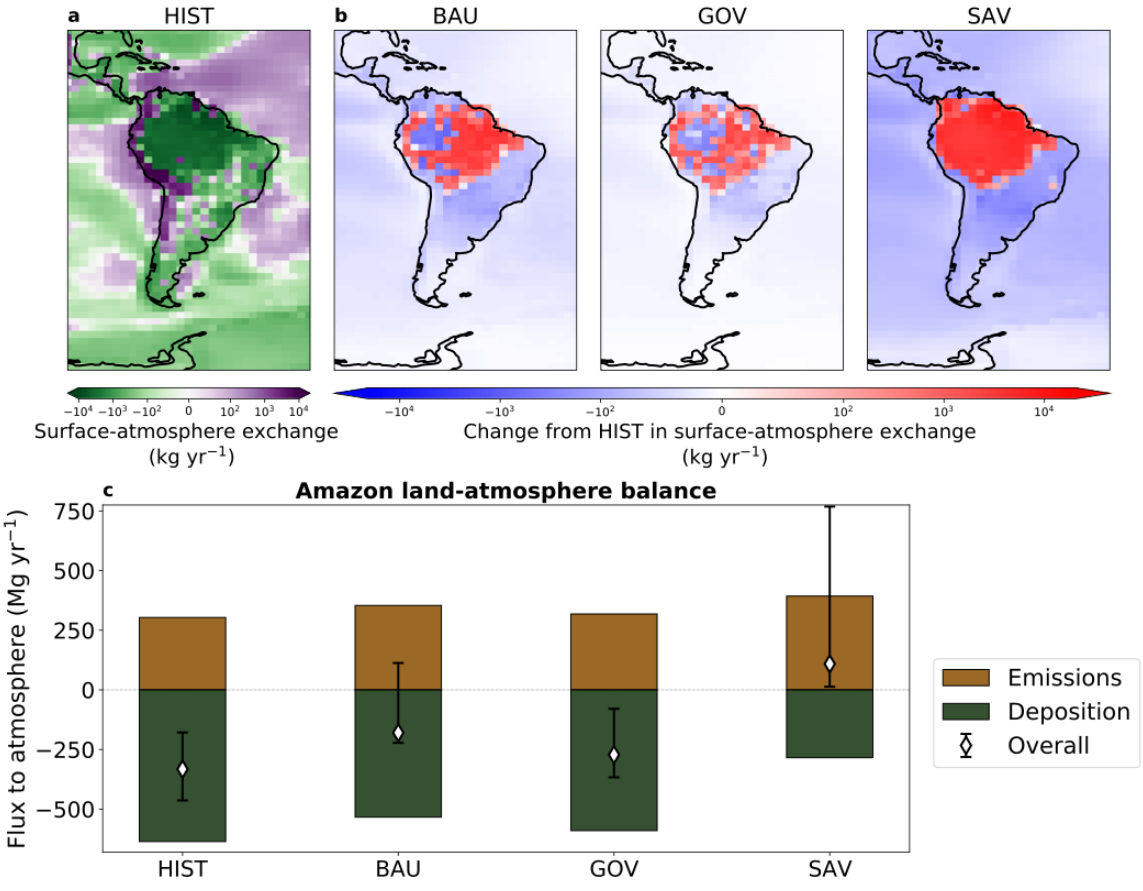

Figure 2. Impacts of Amazon deforestation scenarios on surface-atmosphere Hg exchange. (*a*) The simulated surface-atmosphere exchange (net deposition is negative and net emission is positive) of Hg in the reference simulation (HIST). (*b*) Changes in exchange fluxes from HIST are shown for the deforestation scenarios: Business-as-usual (BAU), Governance (GOV), and Savannization (SAV); negative values refer to increased net fluxes to the surface compared to HIST and positive values refer to increased net fluxes to the atmosphere. (*c*) Total simulated fluxes of Hg emissions and deposition are calculated for the Amazon region in each scenario. White diamonds illustrate the net flux of Hg to the atmosphere (= emissions – deposition) and error bars refer to the 95% confidence interval based on model parameter uncertainties.

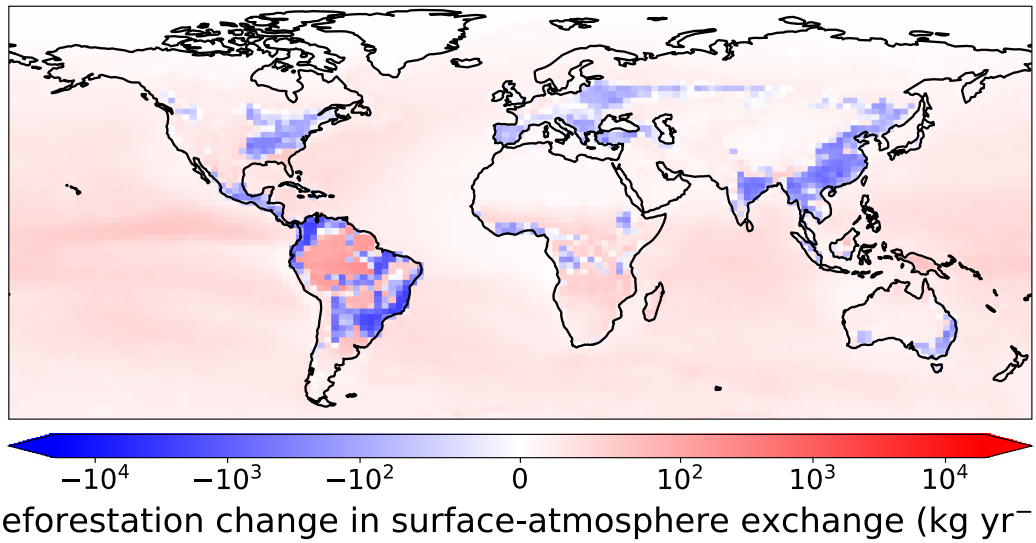

Figure 3. Enhanced land sink of Hg with reforestation. The impact of the potential reforestation (RFR) scenario on surface-atmosphere exchange. The differences from the reference (HIST) simulation are shown, with negative values referring to increased net fluxes to the surface and positive values referring to increased net fluxes to the atmosphere.

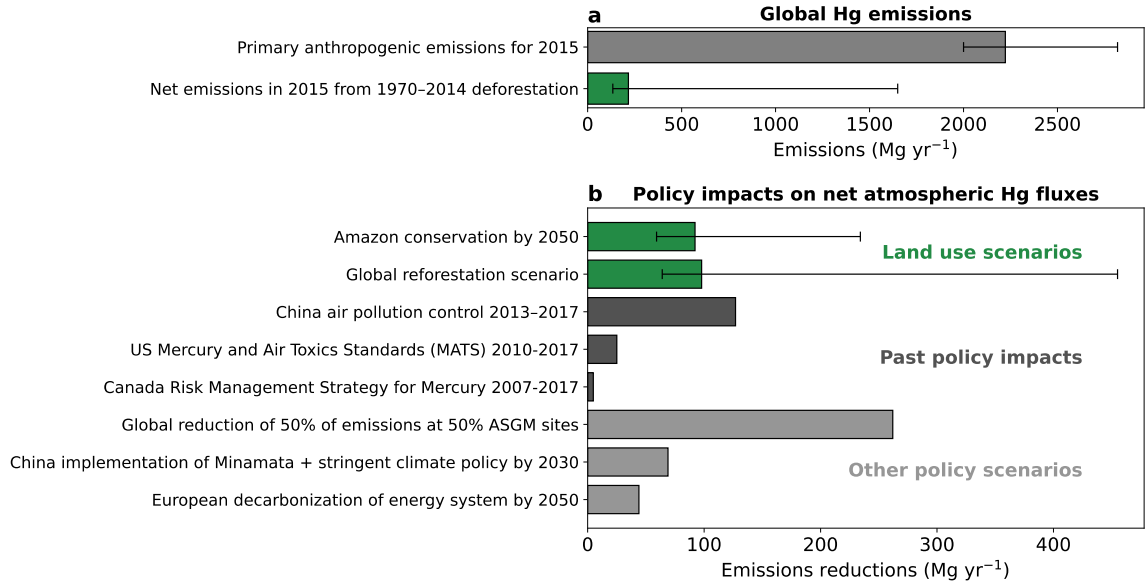

Figure 4. Potential of land use policies to reduce net Hg fluxes to the atmosphere. (*a*) Comparing global 2015 emissions from primary anthropogenic emissions (63–68) and deforestation-driven emissions, assuming a 45-year time horizon (1970–2014 deforested areas). (*b*) Net Hg emissions reductions from land use policies are compared to primary anthropogenic emissions policies, whose impacts have been quantified in the literature (63–68). ASGM refers to artisanal and small-scale gold mining. For land use scenarios, “Amazon conservation by 2050” refers to the net emissions reductions in the 2050 governance (GOV) from the business-as-usual (BAU) simulations and “Global reforestation scenario” compares the net emissions reductions in the reforestation scenario (RFR) compared to the reference simulation (HIST). Error bars refer to the 95% confidence interval based on model parameter uncertainties.

Supplementary Information (SI) for

Deforestation as an anthropogenic driver of mercury pollution

Aryeh Feinberg[a], Martin Jiskra[b], Pasquale Borrelli[c], Jagannath Biswakarma[b,d], and Noelle E. Selin[a,e]

[a] *Institute for Data, Systems, and Society, Massachusetts Institute of Technology, Cambridge, MA, USA*

[b] *Environmental Geosciences, University of Basel, Basel, Switzerland*

[c] *Department of Science, Roma Tre University, Rome, Italy*

[d] *Department of Water Resources and Drinking Water, Eawag, Dübendorf, Switzerland*

[e] *Department of Earth, Atmospheric, and Planetary Sciences, Massachusetts Institute of Technology, Cambridge, MA, USA*

*Correspondence to: arifeinberg@gmail.com (A.F.); martin.jiskra@gmail.com (M.J.)

This PDF file includes:

Section S1. Soil emissions parameterization

We improved the model's parametrization of Hg^0 soil emissions by adopting a new formulation for the parametrization, suggested by Khan et al. (1):

$$E_{\text{soil}} = aC^b R_g^c \quad \text{(S1)}$$

where E_{soil} are soil emissions (ng m^{-2} h^{-1}), C is the concentration of Hg in soils (ng g^{-1}), R_g is the solar radiation flux at the ground (W m^{-2}), and a, b, and c are coefficients.

As in Selin et al. (2), the solar radiation at ground (R_g) is determined by considering attenuation of the solar radiation flux (R_S) by shading from the overhead canopy, parametrized by the leaf area index (LAI):

$$R_g = R_S \exp\left(-\frac{\alpha \text{LAI}}{\cos\theta}\right) \quad \text{(S2)}$$

where α = 0.5, assuming extinction from a random angular distribution of leaves (3) and θ is the solar zenith angle.

We compiled several relevant observational constraints for the parametrization in Tables S1 and S2. Observational studies from the Amazon region (where most of the prior field research has been concentrated) suggest that deforestation has a large impact on soil emissions due to removal of canopy shading, showing factors of 1.8×, 6.7×, and >31× more emissions in forested compared to deforested land plots (Table S1). Observational studies from other regions find a similarly high sensitivity of soil emissions to the presence of forest: open fields in China showed 6–10 times higher Hg emissions than forests (4) and logging in the US flipped the surface-air Hg^0 flux from net deposition to net emissions (–2.2 μg m^{-2} yr^{-1} to +5.5 μg m^{-2} yr^{-1}) (5). For extratropical grassland soil emissions, we use the compiled median values from Zhu et al. (6) and Agnan et al. (7)

We conducted a parameter sweep of a, b, and c, calculating globally-gridded soil emissions using annual solar radiation data (Fig. S1). Sensitivity simulations showed that the ratio of deforested to forested soil emissions in the Amazon (median value 6.7) can tune the exponent for the radiation term (c in Eq. S1), i.e., the response of emissions to canopy shading. The exponent for the soil concentration term (b) was tuned with the ratio of deforested Amazon soil emissions (Table S1) to extratropical grassland soil emissions from the Northern Hemisphere from two review studies (6, 7) (overall Amazon to extratropical ratio of 5.3). Lastly, after these coefficients are tuned, the prefactor a is adjusted so that predicted annual mean emissions match the observed median magnitudes of Amazon deforested soil emissions (23 μg m^{-2} yr^{-1}) and extratropical grassland emissions (4.3 μg m^{-2} yr^{-1}).

We recognize the uncertainties in the observed data used to tune this parametrization, and thus we constructed 100 alternative parametrizations that fit within observed data bounds (Table S5). These parametrizations were applied in offline uncertainty analyses to assess 95% confidence intervals in the fluxes driven by deforestation (Section S4).

Table S1. Literature review of available Hg^0 soil emission flux measurements from the Amazon region, differentiated by land cover type.

Reference	Location	Site	Deforested Hg^0 flux (μg m^{-2} yr^{-1})	Forested Hg^0 flux (μg m^{-2} yr^{-1})	Flux ratio (deforest:forest)
Magarelli and Fostier (8)	Negro River Basin, Brazil	#1	27 ± 9	0.6 ± 1.5	
		#2	19	–1.0 ± 0.8	
		#3	9.8 ± 0.7		
		Mean	18	–0.2	> 31[a]
Almeida et al. (9)	Rondônia, Brazil	#1	79 ± 110	44 ± 18	1.8
Carpi et al. (10)	Acre, Brazil	#1	19 ± 2	2.9 ± 0.8	6.7
		#2	230[b]		
	Median		**23**	**1.8**	**6.7**

[a]lower limit calculated assuming the forested flux is equal to site #1, as site #2 shows negative overall flux; deforested flux assumed as mean.

[b]this site was 2-months post-fire and soil temperatures were still elevated; this flux is excluded from ratio calculations

Table S2. Observational constraints used to tune the soil emissions parametrization.

Constraint	Value	Reference	Coefficient constrained
Amazon deforested soil emissions (μg m^{-2} yr^{-1})	23	Table S1	*a*
Extratropical grassland soil emissions (μg m^{-2} yr^{-1})	4.3†	Zhu et al. (6); Agnan et al. (7)	*a*
Ratio of Amazon to extratropical soil emissions	5.3	(23:4.3)	*b*
Ratio of deforested to forested Amazon soil emissions	6.7	Table S1	*c*

†average of grassland median Hg^0 fluxes from the two independent review studies

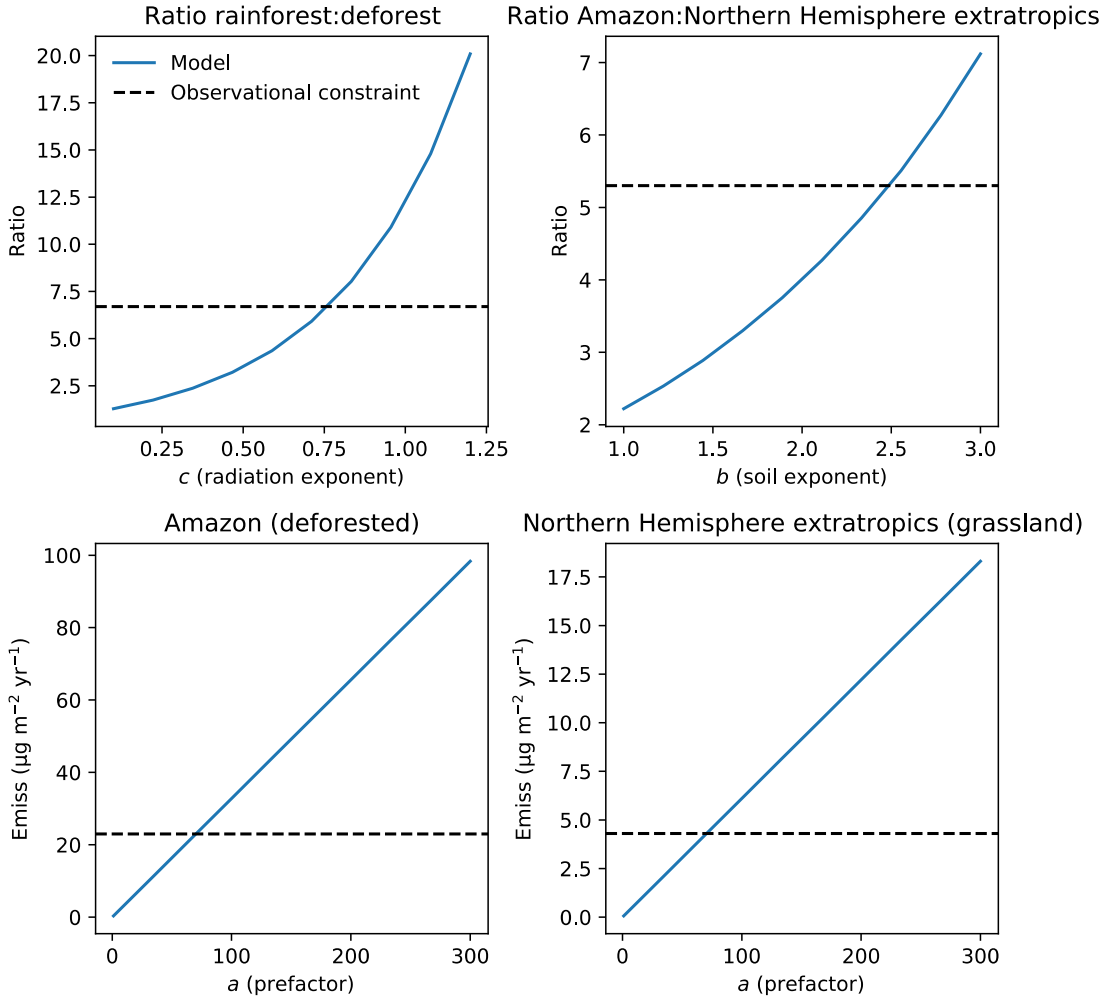

Figure S1. Parameter tuning (Eq. S1) to match observational constraints from Table S2.

The tuning procedure is illustrated in Fig. S1, yielding best matches for a = 71, b = 2.5, and c = 0.76. We compare the gridded annual mean soil emissions from the previous soil emission parametrization (GEOS-Chem v12.8) and the current study (Eq. S1) in Fig. S4. Global annual mean soil Hg^0 emissions in the new parametrizations (954 Mg yr^{-1}) is similar to the predictions from two GEOS-Chem studies (11, 12) using the previous parametrization: 860 ± 440 Mg yr^{-1} and 910 Mg yr^{-1}. The spatial distribution of emissions (Fig. S2) shows a decrease in vegetated regions (e.g., the Amazon and Congo rainforests) and an increase in regions with high soil Hg concentrations (e.g., eastern China).

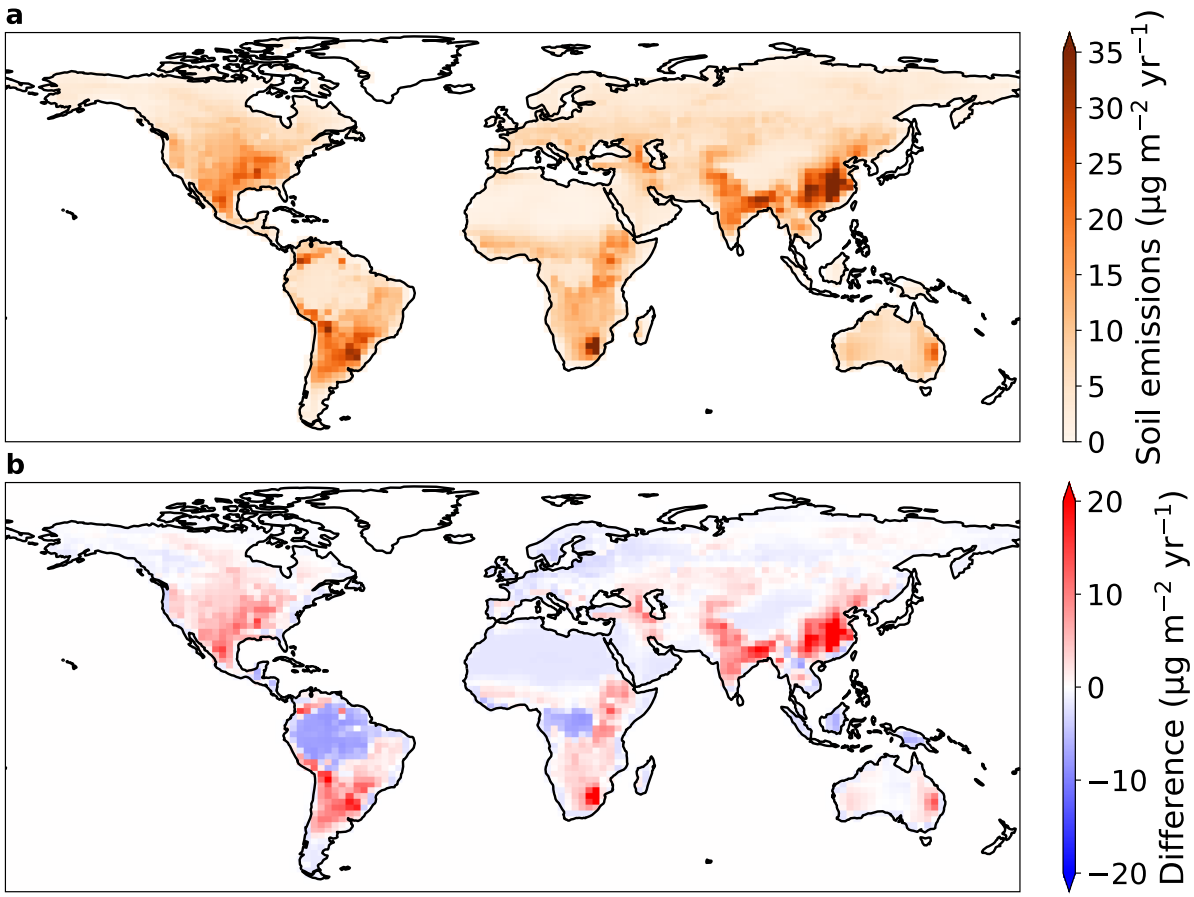

Figure S2. (*a*) Annual mean soil emissions of Hg^0 with the new parametrization. (*b*) Difference between new and old (GEOS-Chem v12.8) soil emissions parametrizations (new minus old).

Section S2. Observational constraints on deforestation Hg fluxes

There are several available sources of information that can be used to validate the deforestation emission factors (EF) calculated by GEOS-Chem (Fig. S4, SI Spreadsheet):

1) *Soil Hg concentration measurements of paired forest-deforested sites*:
Several studies, mainly focused in the Amazon rainforest, have measured the concentrations of Hg soils at deforested sites (C_d) and nearby forest (C_f) plots. For this analysis, we assume that the difference in these soil concentrations is due to mainly the change in atmospheric exchange, which is supported by the magnitude of modeled erosion fluxes (Section S6) and available measurements (5). We use the following equation to convert the difference in these concentrations to a deforestation emission factor of Hg in Mg m^{-2} yr^{-1}:

$$\text{Total EF} = \frac{(C_d - C_f) \times \rho \times h}{t_d} \quad \text{(S3)}$$

where ρ is the density of the soil, h is the depth of the soil layer, and t_d is the time since deforestation. In the US (Nearctic), there have been studies in Ohio (13) and Oregon (14) with measurements of Hg in deforested and forested soils, which we use to calculate deforestation EFs for the Nearctic. For the Amazon, more measurements are available (24 pairs of soil plots) (8–10, 15–25). We compiled a literature database of studies that compared Hg concentrations in deforested Amazonian soils with nearby forest plots (Fig. S3; SI Spreadsheet). Deforested sites show a consistent decrease compared to paired forested sites (*p*-value < 0.001; Wilcoxon signed-rank test), with the median decrease being 25 ng g^{-1} (10^{th}–90^{th} percentile: 2–58 ng g^{-1}). To calculate a deforestation EF for the Amazon, we apply this concentration decrease in Eq. S3 and assume an average Amazon soil density of 1.25 ng g^{-1}, a surface soil layer of 10 cm, and that deforested soils in the literature studies were measured 10 years after deforestation.

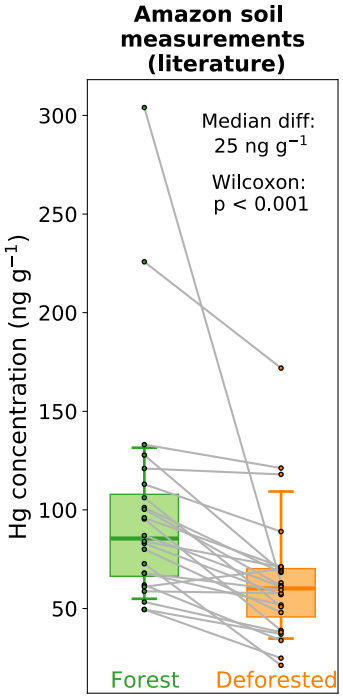

Figure S3. Measured Hg concentrations in forest (green) and deforested (orange) soils (0–20 cm depth) from the literature (*n* = 24) (8–10, 15–25). Box plots show the median values (solid lines), interquartile range (shaded), and 10th and 90th percentiles (whiskers). Gray lines connect paired sites from the same study. Listed *p*-value (<0.001) refers to the Wilcoxon signed-rank test of the null hypothesis that paired forest and deforested sites come from the same distribution.

2) *Terrestrial-atmosphere exchange models validated by Hg observations*:
An estimate for the deforestation EF over China is available from the Wang et al. (26) modeling study. We use their area-averaged mean fluxes over forest and agricultural land cover to calculate a deforestation emission factor:

$$\text{Total EF} = (E_d - D_d) - (E_f - D_f) \quad \text{(S4)}$$

where E_d and E_f are the natural emission fluxes (Mg m^{-2} yr^{-1}) from Chinese agricultural land and forest, and D_d and D_f are the deposition fluxes (Mg m^{-2} yr^{-1}) to Chinese agricultural land and forest. Although this EF estimate is model-based, the Wang et al. (26) model was validated extensively with available terrestrial-atmosphere exchange measurements from China.

3) *Dynamic flux chamber measurements of forested and deforested soils*:
Additional studies investigating the impact of deforestation on atmospheric fluxes quantified the response of soil emissions using dynamic flux chamber measurements (5, 8–10, 27, 28). We compare these measurements to the soil-only EF modeled by GEOS-Chem. The soil emission factors measured by the studies is calculated as the difference between soil emissions (Mg m^{-2} yr^{-1}) over deforested and forested soils:

$$\text{Soil EF} = E_d - E_f \quad \text{(S5)}$$

The comparison between GEOS-Chem simulated deforestation EFs and observation-derived values is summarized in Fig. S4. Observations are only available from three regions (Amazon, China and Nearctic). We found further references investigating the impact of deforestation on Hg for the Palearctic region (29, 30), yet these focused on measuring Hg concentrations in aquatic media and methylation potential rather than soil concentrations or atmospheric exchange. Australian soil measurements (31, 32) have been made before and after vegetation burning events, but do not cover the longer term soil Hg response to deforestation.

The modeled EF estimates and their uncertainties overlap with observation-derived EFs for all 3 regions. If anything, the modeled best estimate used in online simulations is conservative compared to available observations, showing generally lower EFs (Fig. S4). However, it is unclear whether the sparse observations available are representative of the overall region. The modeled EF uncertainty estimates cover 1–2 orders of magnitude, emphasizing the current uncertainties in the response of Hg fluxes to deforestation. The modeled error ranges appear well-calibrated in that they cover a similar

range as the variability in observation-derived fluxes. Figure S4 also reveals the regions where no observations of the impact of deforestation on Hg cycling are currently available. Specifically, the Afrotropic and Indomalayan domains would be priorities for future measurement campaigns, given the current impact of deforestation in those regions (Fig. 1). It remains unknown whether Southeast Asian and African rainforests show similarly high levels of Hg in litterfall as the Amazon rainforest (33).

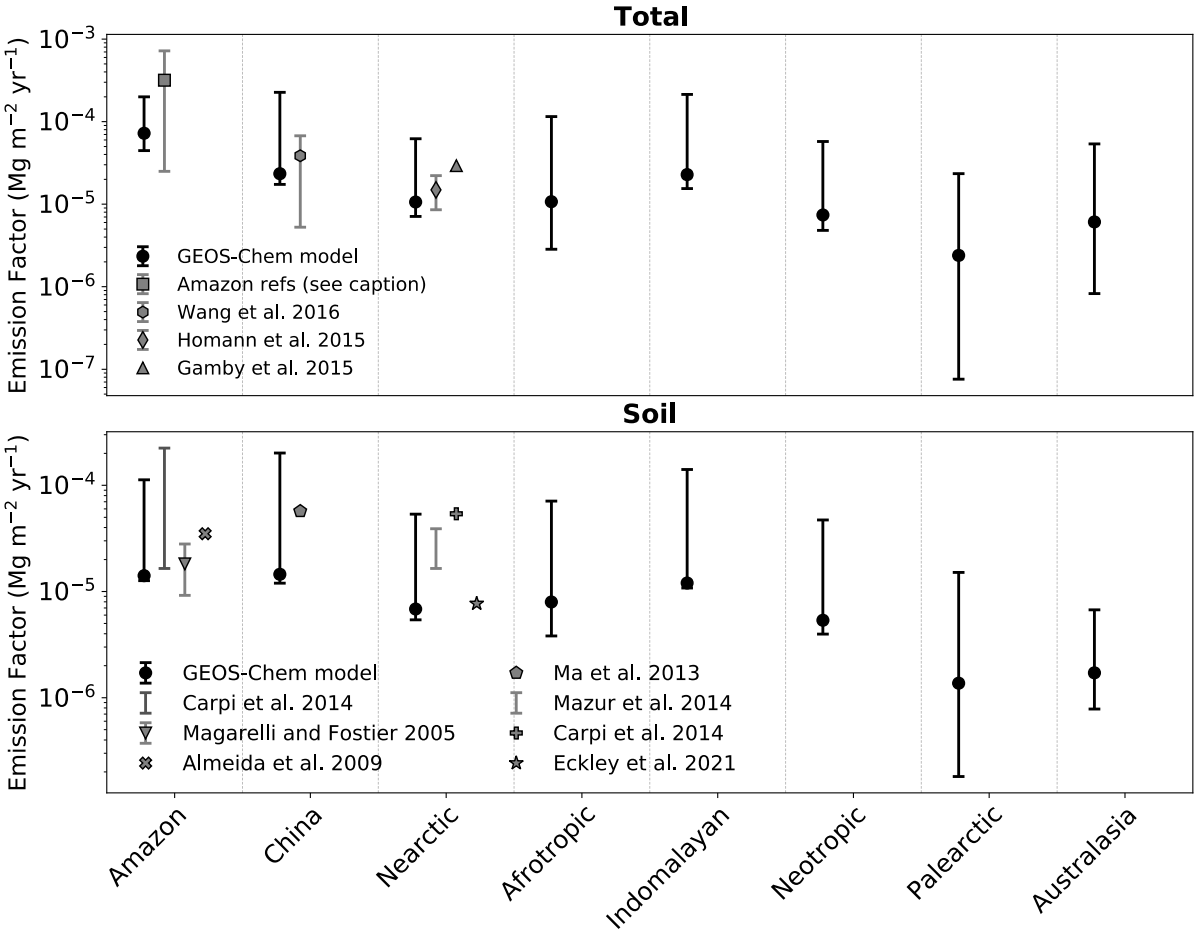

Figure S4. Comparison between modeled and observation-derived net emission factors (EFs) for deforestation in different regions. The upper panel shows total EFs and the lower panel shows the soil Hg^0 emissions component of deforestation EFs. Modeled circles show the best estimate (online simulations), while error bars show the 95% confidence interval due to model parameter uncertainties (calculated in offline simulations, Section S4). Observation estimates are from refs. (5, 8–10, 13–28), with the Amazon Total EF estimate based on measurements in Fig. S3. Observed error bars refer to uncertainty ranges when multiple plots were measured within a study (see SI spreadsheet for full calculations).

Section S3. Global deforestation-driven emissions estimates

We use perturbation simulations in which a set area within a region is deforested to calculate each deforestation EF. Using the Amazon deforestation scenario experiments, we explored the validity of our assumption to linearly relate the deforested area to the change in land-air fluxes (Fig. S5). In these four simulations — the reference simulation with 2003 forest cover (HIST), governance scenario for 2050 (GOV), business-as-usual for 2050 (BAU), and savannization (SAV) — different areas (both in spatial pattern and extent) were deforested in the Amazon region. The total fluxes from the Amazon basin for Hg^0 dry deposition, soil Hg^0 emissions, and the overall land-air balance of Hg all respond linearly (R^2>0.98) to the magnitude of the deforested area. Therefore, the approach of calculating deforestation EFs and scaling these with deforested areas would likely not be highly sensitive to the spatial distribution and amount of deforestation.

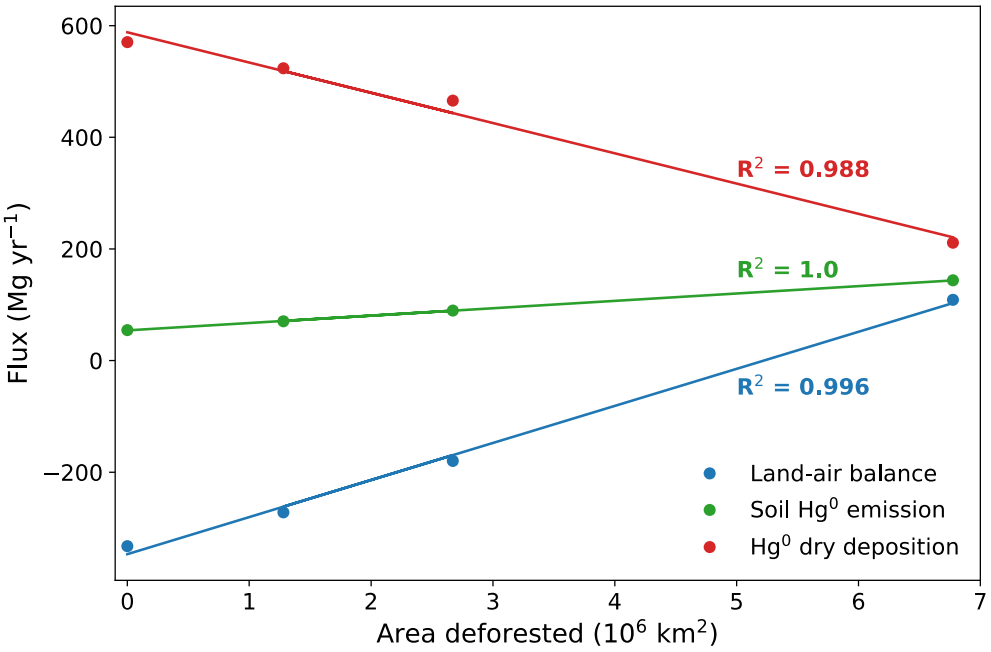

Figure S5. Relationship between land-air fluxes and the area deforested in GEOS-Chem simulations for the Amazon rainforest. Fluxes are averaged over the Amazon rainforest domain and listed R^2 values refer to linear models.

Additional data related to the calculation of historical deforestation-driven emissions of Hg are presented in this section. The maps defining the regions used in this study is shown in Fig. S6. Table S3 tabulates the results from the perturbation simulations for the different regions and the resultant emission factors. Fig. S7 explores the impact of choosing different time horizons for the deforestation area on the calculated Hg emissions globally and by country. Fig. S8 shows the map of Hg deforestation-driven emissions, assuming a 45 year time horizon (deforestation area of 1970–2014 from the LUH2 dataset (34)).

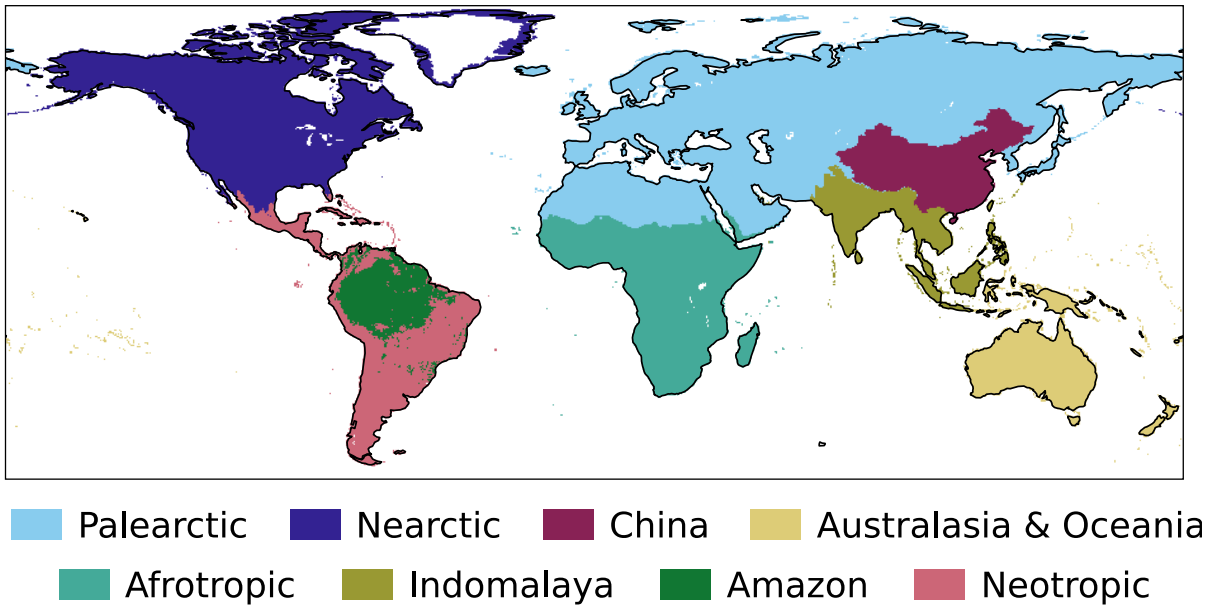

Figure S6. Definition of regions used to calculate the deforestation emission factors.

Table S3. Results from the deforestation perturbation simulations in GEOS-Chem for determining the response of land-air fluxes to deforesting a specified area. Emissions factors are listed with the 95% confidence interval calculated in offline simulations assessing the uncertainties due to model parameters (Section S4).

Realm	Area deforested (km^2)	Change in emissions ($Mg\ yr^{-1}$)	Change in deposition ($Mg\ yr^{-1}$)	Change in net emissions ($Mg\ yr^{-1}$)	Emissions factor ($Mg\ m^{-2}\ yr^{-1}$) [95% confidence interval]
Afrotropic	3 644 969	29.1	-10.0	39.1	1.1×10^{-5} [2.8×10^{-6} to 1.2×10^{-4}]
Neotropic	2 422 577	13.0	-4.9	17.9	7.4×10^{-6} [4.8×10^{-6} to 5.7×10^{-5}]
Indomalaya	2 626 474	31.6	-28.3	59.9	2.3×10^{-5} [1.5×10^{-5} to 2.1×10^{-4}]
Palearctic	4 221 663	5.8	-4.3	10.1	2.4×10^{-6} [7.6×10^{-8} to 2.3×10^{-5}]
Nearctic	4 606 898	31.6	-17.4	48.9	1.1×10^{-5} [7.1×10^{-6} to 6.2×10^{-5}]
Australasia	1 088 250	1.9	-4.8	6.6	6.1×10^{-6} [8.3×10^{-7} to 5.4×10^{-5}]
China	1 141 180	16.6	-10.1	26.7	2.3×10^{-5} [1.7×10^{-5} to 2.3×10^{-4}]
Amazon	6 775 429	96.2	-394.0	490.2	7.2×10^{-5} [4.5×10^{-5} to 2.0×10^{-4}]

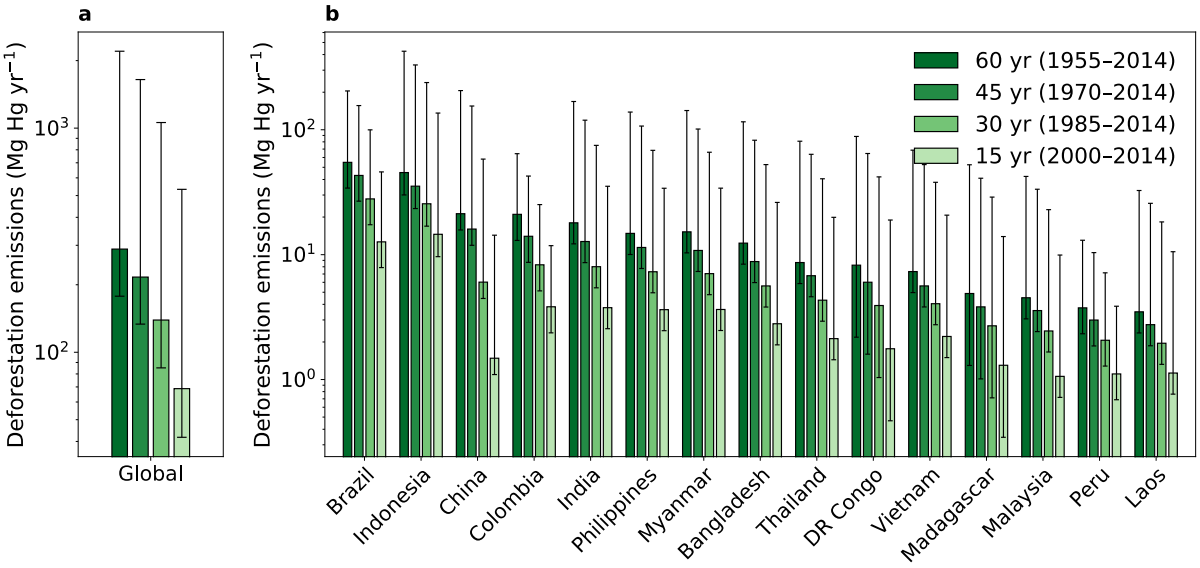

Figure S7. (*a*) Global and (*b*) country-level deforestation emissions of Hg for the top 15 emitting countries. Results are summarized accumulating deforested area over different time horizons (15 years, 30 years, 45 years, and 60 years) before 2015. Error bars refer to the 95% confidence interval based on the uncertainty in model parameters (Section S4).

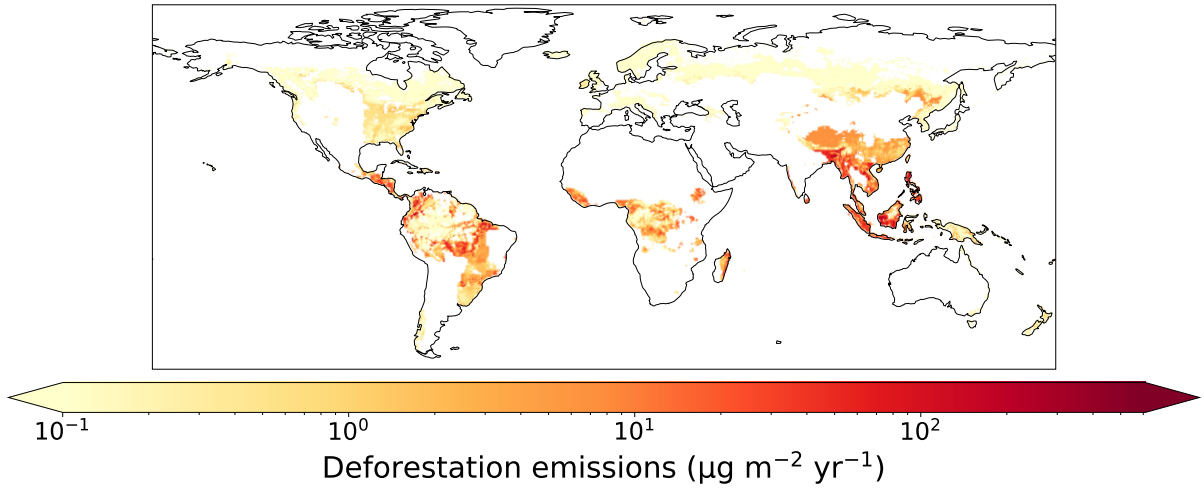

Figure S8. Map of net emissions of Hg from deforestation calculated over a 45 year time horizon before 2015 (1970–2014), using deforested area from the LUH2 dataset (34).

Section S4. Parameters used in uncertainty analysis

Table S4. Parameter uncertainty bounds applied in the uncertainty analysis.

Parameter	Min	Max	Units	Distribution	Comment
Soil emission parametrization	1	100	-	Uniform	Integer representing one of 100 reasonable parametrizations calculated within the range of observed uncertainties (Table S5)
Percentile of replaced LAI when building scenarios	10	90	-	Uniform	e.g., deforested Amazon area is assigned 10th percentile LAI of HIST savanna, instead of mean for default estimate
Dry deposition Hg^0 reactivity (f_0) Amazon rainforest	10^{-2}	0.5	-	Loguniform	Based on Feinberg et al. (33), within range of available vegetation uptake measurements
Dry deposition Hg^0 reactivity (f_0) other rainforests	10^{-5}	0.2	-	Loguniform	Based on Feinberg et al. (33); no available measurements from other rainforests, leading to wider f_0 uncertainty
Dry deposition Hg^0 reactivity (f_0) elsewhere	10^{-5}	5×10^{-5}	-	Uniform	Based on Feinberg et al. (33), within range of available vegetation uptake measurements
Biomass burning emission factor for Amazon	350	615	μg m^{-2}	Uniform	Estimated range in literature (10, 35, 36)

Table S5. Bounds of observed parameters used to calculate 100 reasonable soil emission parametrizations, which are then applied in the uncertainty analysis (Table S4).

Parameter	Min	Max	Units	Comment
Ratio of deforested to forested Amazon soil emissions	1.8	31	-	Range from Table S1
Ratio of Amazon to extratropical soil emissions	3.5	8	-	Assume 50% error from Table S2
Extratropical grassland soil emissions	3.5	11.4	μg m^{-2} yr^{-1}	Grasslands and background soil range from literature reviews (6, 7)
Deforested Amazon soil emissions	9.8	79	μg m^{-2} yr^{-1}	Range from Table S1

Section S5. Scenarios for Amazon deforestation and global reforestation

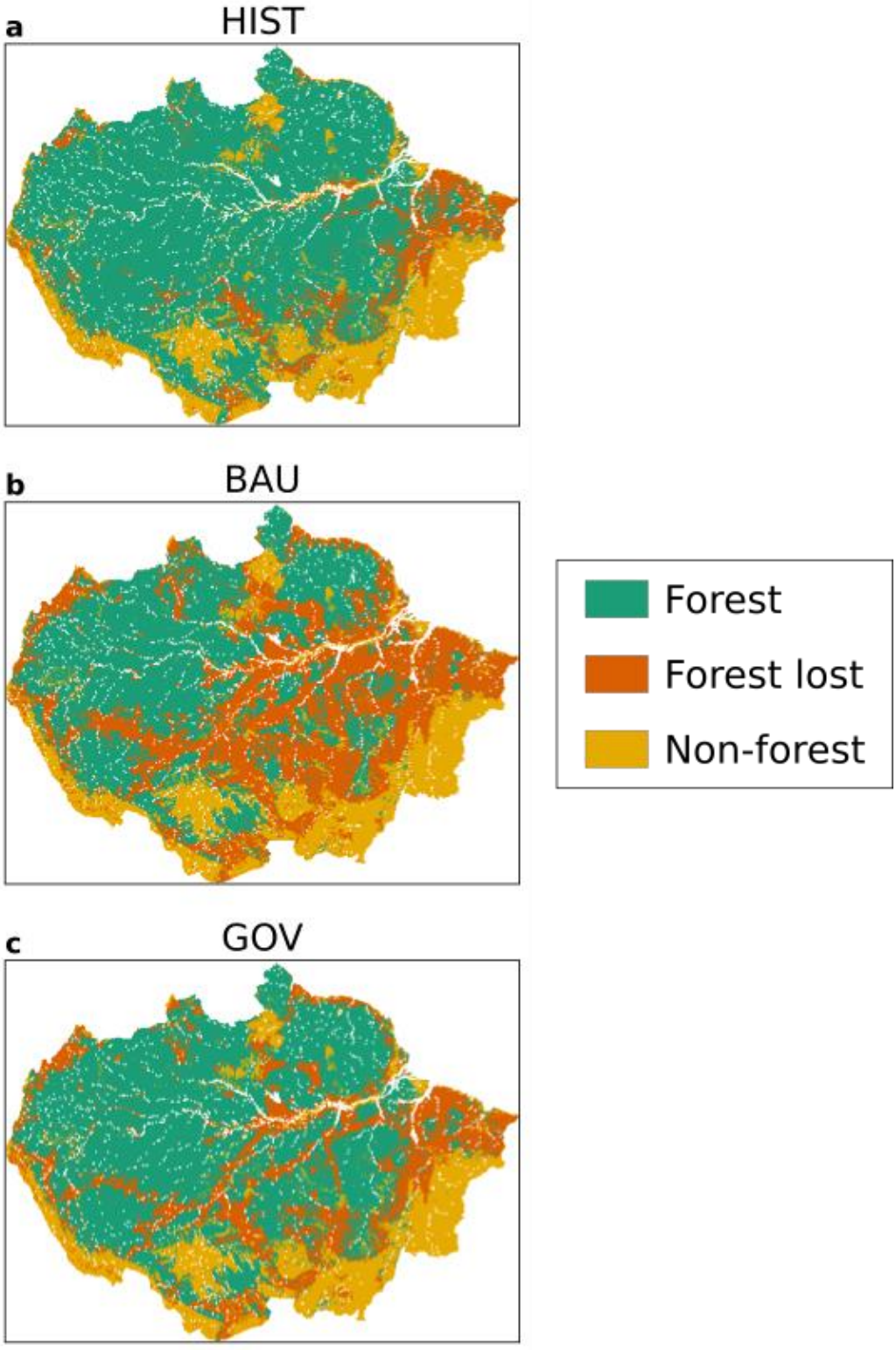

Figure S9. Map of the Amazon basin showing the area of forest, forest loss and rangeland and agriculture in (*a*) HIST; and projections for 2050 in (*b*) Business as Usual (BAU) and (*c*) Governance (GOV) scenarios (replotted from Soares-Filho et al. (37) data).

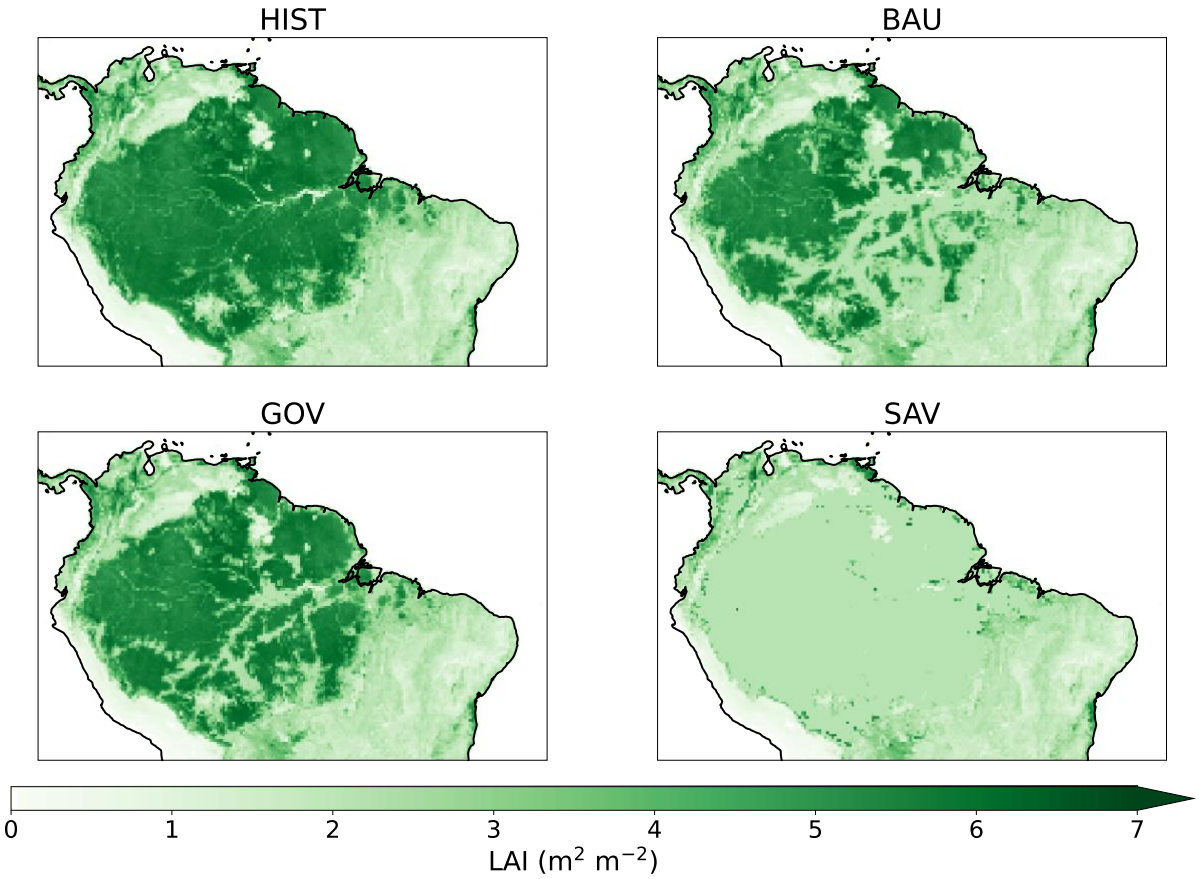

Figure S10. Annual mean leaf area index (LAI) maps for the Amazon deforestation scenarios at 0.25° × 0.25° resolution. The simulations names refer to the following scenarios: reference (HIST), Business-as-usual (BAU), Governance (GOV), and Savannization (SAV).

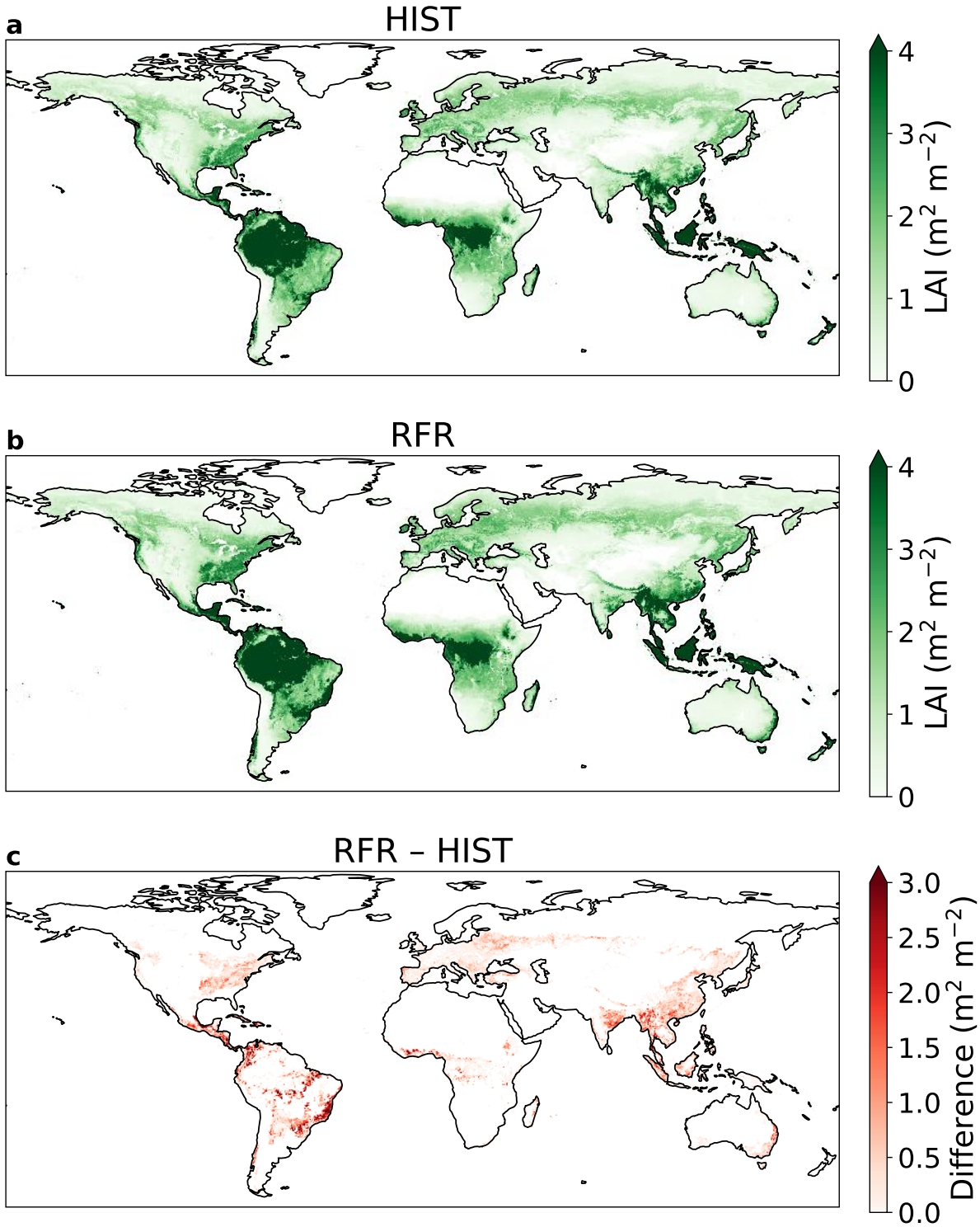

Figure S11. Annual mean leaf area index (LAI) maps at 0.25 × 0.25° resolution for: (*a*) the reference (HIST) scenario (*b*) Reforestation scenario (RFR) (*c*) Difference between RFR and HIST.

Section S6. Impact of Amazon deforestation on erosion

Previous field studies (15, 38) have suggested that erosion of Hg is increased after deforestation in the Amazon, measuring enhanced runoff of Hg in deforested catchments. We estimated the change in soil displacement by water erosion (soil erosion) in the Amazon deforestation scenarios using the RUSLE-based (39) modeling platform Global Soil Erosion Modeling (GloSEM) (40, 41). As a detachment-limited soil erosion prediction model, GloSEM estimates soil erosion (expressed as a mass of soil lost per unit area and time, Mg ha^{-1} yr^{-1}) due to inter-rill and rill erosion processes by multiplication of six contributing factors. The modeling scheme follows the same principle of most

RUSLE-type models or more complex catchment-scale process-based models, with a driving force (erosivity of the climate, R), a resistance term (erodibility of the soil, K) and other factors representing the farming choice, i.e., topographical conformation of the field (LS), cropping system (C), and soil conservation practices (P).

Our approach for calculating soil erosion in the Amazon scenarios is similar to the GloSEM parametrization adopted by Borrelli et al. (40, 41) to estimate human-induced soil erosion change between 2001 and 2070 at a global scale. The horizontal resolution of the native soil erosion modeling is 250 × 250 m. The calculation of erosivity (R), erodiblity (K), topographical conformation of the field (LS), and soil conservation practices (P) factors are described in Borrelli et al. (40, 41). We acknowledge that the calculation of erosion model factors for the Amazon rainforest may be associated with higher uncertainties than other regions due to the lower density in meteorological stations (42) and soil sampling sites (43). For this study, we adapted the computation of the land cover and management factor (C-factor), which measures the combined effect of vegetation cover and cropping system variables on the soil erosion process. We parametrize the C-factor according to two layers of information: 1) the spatial dimension of land use classes according to the deforestation scenarios from Soares-Filho et al. (37) (described below); 2) the vegetation condition in each land use class using the MODIS MOD44B Vegetation Continuous Fields product (VCF) (~250m spatial resolution) as a proxy to quantify (i) surface vegetation cover, (ii) tree cover, and (iii) bare soil. As we focus our analysis on comparing the forest coverage in the years 2003 and 2050, the baseline vegetation condition is given by the average VCF values over the years 2000, 2001 and 2002. The C-factor for noncropland areas (C_{nc}) is estimated in two steps. First, a preliminary C-factor (C_p) not considering tree cover is calculated as:

$$C_p = C_{min} + \left((C_{max} - C_{min})\,\mathrm{NVS}\right) \qquad \text{(S6)}$$

where the C_{min} (0.01) and C_{max} (0.15) express the potential range in C-factor values for dense to sparse grassland cover. NVS (non-vegetated surface) is spatially defined using the MODIS MOD44B VCF data normalized to a range from 0 to 1 and describes the percentage of ground covered by any vegetation type. For the NVS, the C-factor is set to 0.5. Within the next step, the final land cover and management C-factor for non-croplands (C_{nc}) is computed including the tree coverage (TC) defined using the MODIS MOD44B VCF normalized to range from 0 to 1:

$$C_{nc} = C_{p\,min} + \left(\left(C_{p\,max} - C_{p\,min}\right)\mathrm{TC}\right) \qquad \text{(S7)}$$

where the $C_{p\,min}$ and $C_{p\,max}$ values are set to 0.0001 (100% canopy cover) and 0.009 (sparse forest vegetation).

While the deforestation scenarios proposed by Soares-Filho et al. (37) provide a spatial quantification of the forest losses between 2003 and 2050, the annual shares of conversion from forest to grassland or cropland are separate from the annual projection of the Land-Use Harmonization (LUH2) data (34), which provides fractional land-use patterns (850-2100) at 0.25° × 0.25° resolution. The downscaling of the LUH2 fractional cropland and grassland data from 0.25° × 0.25° resolution to the 250 m × 250 m resolution of the erosion model is performed through a probabilistic land use allocation scheme based on classification rules applied to auxiliary information (i.e., a crop suitability index, more detail in Borrelli et al. (40)). Finally, the C-factor of the cropland is defined at sub-national administrative level (Global Administrative Unit Levels) based on the Food and Agriculture Organization's (FAO) FAOSTAT database, which allowed to statistically describe typical crop rotations in each region. The C-factor of the croplands ranges from 0.131 (Northern Suriname) to 0.332 (Northeast Brazil).

Following the assumption of Lugato et al. (44) for eroded carbon, we assume that 30% of the eroded soil flux is not redeposited on land and enters riverine systems. The fraction of eroded Hg which enters aquatic systems is uncertain, depending on hillslopes dynamics and flow patterns that are not explicitly modeled by the RUSLE-based framework, as well as whether Hg would be selectively eroded relative to carbon. We recognize that this assumption introduces uncertainty into our calculations, and assume that the fraction of eroded soil which enters riverine systems can vary between 5–47%, the range reported by Van Oost et al. (45) We calculate the eroded flux of Hg from land by multiplying the soil flux by the median Hg concentration in Amazon forested soils from a literature review (86 ng g^{-1}; see SI Spreadsheet).

For each Amazon scenario, we tabulate the Hg erosion fluxes in Table S6. Erosion in the HIST scenario represents a flux of 64 Mg yr^{-1} (uncertainty range: 11–100 Mg yr^{-1}). Erosion is enhanced in the deforestation scenarios, ranging from +14% increase in GOV to a 96% increase in the extreme SAV scenario. The absolute magnitudes of erosion flux changes are smaller than the perturbations in the land-air flux, driven by changes in Hg^0 soil emissions and dry deposition (Table S6). Overall,

perturbations to the erosion flux are approximately 14% of the perturbations to the land-air flux due to deforestation. A previous field study (5) has also suggested that the majority of flux changes after deforestation occurs through atmospheric exchange (97%) rather than erosion to riverine systems. Therefore, the land-air changes to the fluxes play the larger role in the impact of deforestation on the mass balance of Hg in soils. Nevertheless, changes to erosion will affect downstream Hg concentrations and the methylation potential after deforestation (5, 29), which would be important to consider when assessing the impact of deforestation on local ecosystems.

Table S6. Soil erosion fluxes for the Amazon basin calculated by the erosion model GloSEM. The simulations names refer to the following scenarios: reference (HIST), Business-as-usual (BAU), Governance (GOV), and Savannization (SAV).

Scenario	**HIST**	**BAU**	**GOV**	**SAV**
Soil loss (Mt yr^{-1})	2467	3276	2816	4834
30% of soil loss (Mt yr^{-1})[a]	740	983	845	1450
[5%–47%]	[123–1159]	[164–1540]	[141–1323]	[242–2272]
Hg erosion (Mg yr^{-1})	64	85	73	125
[uncertainty range]	[11–100]	[14–132]	[12–114]	[21–195]
Change from HIST (Mg yr^{-1})	-	21	9	61
(relative change)		(+33%)	(+14%)	(+96%)
Land-air flux change from HIST	-	153	61	441
(Mg yr^{-1})				

[a] This is the flux assumed to be entering riverine systems

Section S7. Impacts on atmospheric Hg concentrations

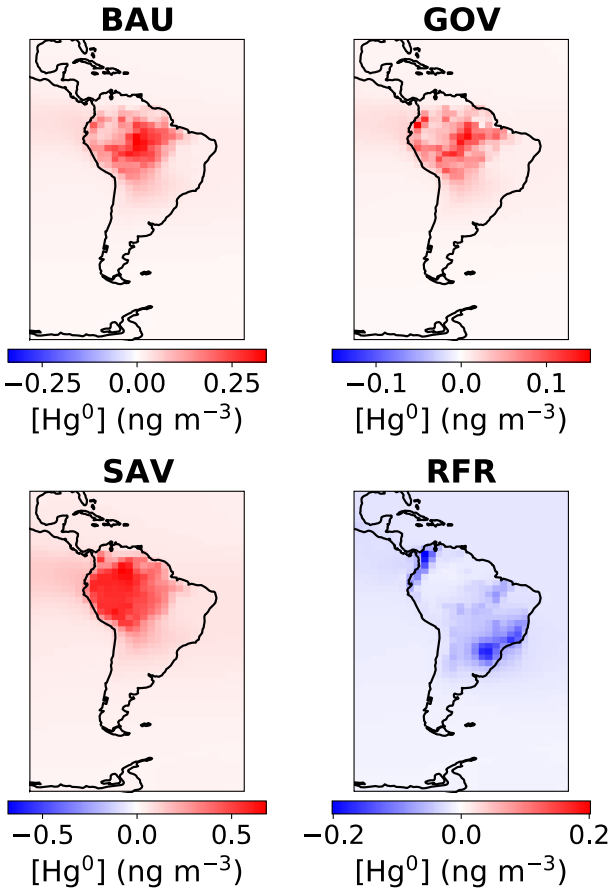

Figure S12. Annual mean differences in simulated atmospheric Hg^0 concentration at the surface between scenarios — Business-as-usual (BAU), Governance (GOV), Savannization (SAV), and global reforestation (RFR) — and the HIST reference simulation.

Supplementary References

1. T. R. Khan, D. Obrist, Y. Agnan, N. E. Selin, J. A. Perlinger, Atmosphere-terrestrial exchange of gaseous elemental mercury: parameterization improvement through direct comparison with measured ecosystem fluxes. *Environ. Sci.: Processes Impacts* **21**, 1699–1712 (2019).
2. N. E. Selin, *et al.*, Global 3-D land-ocean-atmosphere model for mercury: Present-day versus preindustrial cycles and anthropogenic enrichment factors for deposition. *Global Biogeochem. Cycles* **22**, GB2011 (2008).
3. M. M. Verstraete, Radiation transfer in plant canopies: Transmission of direct solar radiation and the role of leaf orientation. *J. Geophys. Res.* **92**, 10985 (1987).
4. J. Zhou, Z. Wang, X. Zhang, C. T. Driscoll, C.-J. Lin, Soil–atmosphere exchange flux of total gaseous mercury (TGM) at subtropical and temperate forest catchments. *Atmos. Chem. Phys.* **20**, 16117–16133 (2020).
5. C. S. Eckley, C. Eagles-Smith, M. T. Tate, D. P. Krabbenhoft, Surface-air mercury fluxes and a watershed mass balance in forested and harvested catchments. *Environmental Pollution* **277**, 116869 (2021).
6. W. Zhu, *et al.*, Global observations and modeling of atmosphere–surface exchange of elemental mercury: a critical review. *Atmos. Chem. Phys.* **16**, 4451–4480 (2016).
7. Y. Agnan, T. Le Dantec, C. W. Moore, G. C. Edwards, D. Obrist, New Constraints on Terrestrial Surface–Atmosphere Fluxes of Gaseous Elemental Mercury Using a Global Database. *Environ. Sci. Technol.* **50**, 507–524 (2016).
8. G. Magarelli, A. Fostier, Influence of deforestation on the mercury air/soil exchange in the Negro River Basin, Amazon. *Atmos. Environ.* **39**, 7518–7528 (2005).
9. M. D. Almeida, R. V. Marins, H. H. M. Paraquetti, W. R. Bastos, L. D. Lacerda, Mercury degassing from forested and open field soils in Rondônia, Western Amazon, Brazil. *Chemosphere* **77**, 60–66 (2009).
10. A. Carpi, A. H. Fostier, O. R. Orta, J. C. dos Santos, M. Gittings, Gaseous mercury emissions from soil following forest loss and land use changes: Field experiments in the United States and Brazil. *Atmos. Environ.* **96**, 423–429 (2014).
11. S. Song, *et al.*, Top-down constraints on atmospheric mercury emissions and implications for global biogeochemical cycling. *Atmos. Chem. Phys.* **15**, 7103–7125 (2015).
12. H. M. Horowitz, *et al.*, A new mechanism for atmospheric mercury redox chemistry: implications for the global mercury budget. *Atmos. Chem. Phys.* **17**, 6353–6371 (2017).
13. R. L. Gamby, C. R. Hammerschmidt, D. M. Costello, C. H. Lamborg, J. R. Runkle, Deforestation and cultivation mobilize mercury from topsoil. *Science of The Total Environment* **532**, 467–473 (2015).
14. P. S. Homann, R. L. Darbyshire, B. T. Bormann, B. A. Morrissette, Forest Structure Affects Soil Mercury Losses in the Presence and Absence of Wildfire. *Environ. Sci. Technol.* **49**, 12714–12722 (2015).
15. A. H. Fostier, *et al.*, Mercury fluxes in a natural forested Amazonian catchment (Serra do Navio, Amapá State, Brazil). *Sci. Total Environ.* **260**, 201–211 (2000).
16. J. R. Gerson, *et al.*, Amazon forests capture high levels of atmospheric mercury pollution from artisanal gold mining. *Nat Commun* **13**, 559 (2022).
17. M. D. Almeida, L. D. Lacerda, W. R. Bastos, J. C. Herrmann, Mercury loss from soils following conversion from forest to pasture in Rondônia, Western Amazon, Brazil. *Environmental Pollution* **137**, 179–186 (2005).
18. L. D. Lacerda, M. de Souza, M. G. Ribeiro, The effects of land use change on mercury distribution in soils of Alta Floresta, Southern Amazon. *Environmental Pollution* **129**, 247–255 (2004).
19. A. Béliveau, M. Lucotte, R. Davidson, L. O. do Canto Lopes, S. Paquet, Early Hg mobility in cultivated tropical soils one year after slash-and-burn of the primary forest, in the Brazilian Amazon. *Science of The Total Environment* **407**, 4480–4489 (2009).
20. A. Béliveau, *et al.*, Reduction of soil erosion and mercury losses in agroforestry systems compared to forests and cultivated fields in the Brazilian Amazon. *Journal of Environmental Management* **203**, 522–532 (2017).
21. C. Patry, R. Davidson, M. Lucotte, A. Béliveau, Impact of forested fallows on fertility and mercury content in soils of the Tapajós River region, Brazilian Amazon. *Science of The Total Environment* **458–460**, 228–237 (2013).
22. I. Comte, *et al.*, Impacts of Land Uses on Mercury Retention in Long-Time Cultivated Soils, Brazilian Amazon. *Water Air Soil Pollut* **224**, 1515 (2013).
23. N. Mainville, *et al.*, Decrease of soil fertility and release of mercury following deforestation in the Andean Amazon, Napo River Valley, Ecuador. *Science of The Total Environment* **368**, 88–98 (2006).

24. M. Roulet, *et al.*, The geochemistry of mercury in central Amazonian soils developed on the Alter-do-Chão formation of the lower Tapajós River Valley, Pará state, Brazil. *Science of The Total Environment* **223**, 1–24 (1998).
25. J. C. Wasserman, R. C. Campos, S. de S. Hacon, R. A. Farias, S. M. Caires, Mercury in soils and sediments from gold mining liabilities in Southern Amazonia. *Quím. Nova* **30** (2007).
26. X. Wang, *et al.*, Emission-dominated gas exchange of elemental mercury vapor over natural surfaces in China. *Atmos. Chem. Phys.* **16**, 11125–11143 (2016).
27. M. Mazur, *et al.*, Gaseous mercury fluxes from forest soils in response to forest harvesting intensity: A field manipulation experiment. *Science of The Total Environment* **496**, 678–687 (2014).
28. M. Ma, D. Wang, R. Sun, Y. Shen, L. Huang, Gaseous mercury emissions from subtropical forested and open field soils in a national nature reserve, southwest China. *Atmospheric Environment* **64**, 116–123 (2013).
29. K. Eklöf, R. Lidskog, K. Bishop, Managing Swedish forestry's impact on mercury in fish: Defining the impact and mitigation measures. *Ambio* **45**, 163–174 (2016).
30. H. A. De Wit, *et al.*, Forest harvest effects on mercury in streams and biota in Norwegian boreal catchments. *Forest Ecology and Management* **324**, 52–63 (2014).
31. J. Abraham, K. Dowling, S. Florentine, Effects of prescribed fire and post-fire rainfall on mercury mobilization and subsequent contamination assessment in a legacy mine site in Victoria, Australia. *Chemosphere* **190**, 144–153 (2018).
32. D. Howard, *et al.*, Investigation of mercury emissions from burning of Australian eucalypt forest surface fuels using a combustion wind tunnel and field observations. *Atmospheric Environment* **202**, 17–27 (2019).
33. A. Feinberg, T. Dlamini, M. Jiskra, V. Shah, N. E. Selin, Evaluating atmospheric mercury (Hg) uptake by vegetation in a chemistry-transport model. *Environ. Sci.: Processes Impacts* **24**, 1303–1318 (2022).
34. G. C. Hurtt, *et al.*, Harmonization of global land use change and management for the period 850–2100 (LUH2) for CMIP6. *Geosci. Model Dev.* **13**, 5425–5464 (2020).
35. P. A. M. Michelazzo, A. H. Fostier, G. Magarelli, J. C. Santos, J. A. de Carvalho, Mercury emissions from forest burning in southern Amazon. *Geophys. Res. Lett.* **37**, L09809 (2010).
36. J. J. Melendez-Perez, *et al.*, Soil and biomass mercury emissions during a prescribed fire in the Amazonian rain forest. *Atmospheric Environment* **96**, 415–422 (2014).
37. B. S. Soares-Filho, *et al.*, Modelling conservation in the Amazon basin. *Nature* **440**, 520–523 (2006).
38. M. Roulet, *et al.*, Effects of Recent Human Colonization on the Presence of Mercury in Amazonian Ecosystems. *Water Air Soil Pollut.* **112**, 297–313 (1999).
39. K. G. Renard, G. R. Foster, G. A. Weesies, D. K. McCool, D. C. Yoder, Predicting soil erosion by water: A guide to conservation planning with the Revised Universal Soil Loss Equation (RUSLE). *Agriculture handbook* **703** (1997).
40. P. Borrelli, *et al.*, Land use and climate change impacts on global soil erosion by water (2015-2070). *Proc. Natl. Acad. Sci. U.S.A.* **117**, 21994–22001 (2020).
41. P. Borrelli, *et al.*, An assessment of the global impact of 21st century land use change on soil erosion. *Nat Commun* **8**, 2013 (2017).
42. P. Panagos, *et al.*, Global rainfall erosivity assessment based on high-temporal resolution rainfall records. *Sci Rep* **7**, 4175 (2017).
43. T. Hengl, *et al.*, SoilGrids1km — Global Soil Information Based on Automated Mapping. *PLoS ONE* **9**, e105992 (2014).
44. E. Lugato, *et al.*, Soil erosion is unlikely to drive a future carbon sink in Europe. *Sci. Adv.* **4**, eaau3523 (2018).
45. K. Van Oost, *et al.*, The Impact of Agricultural Soil Erosion on the Global Carbon Cycle. *Science* **318**, 626–629 (2007).